

India–Eurasia convergence speed-up by passive-margin sediment subduction

<https://doi.org/10.1038/s41586-024-08069-6>

Hao Zhou¹, Jiashun Hu^{1,2✉}, Luca Dal Zilio^{3,4}, Ming Tang⁵, Keqing Li¹ & Xiumian Hu⁶

Received: 13 June 2023

Accepted: 18 September 2024

Published online: 6 November 2024

Open access

 Check for updates

The fast increase of convergence rate between India and Eurasia around 65 million years ago (Ma)—from approximately 8 cm yr⁻¹ to a peak rate of approximately 18 cm yr⁻¹—remains a complex geological event to explain^{1–8}, given the inherent uncertainty surrounding the tectonic history and the intricate interplay of forces influencing plate speed^{9–11}. Here we use a combination of geochemical analysis and geodynamic modelling to propose that this rapid convergence can be explained by sediment subduction derived from the northern Indian passive margin. Through isotope and trace element analysis, we find an enhanced contribution of terrigenous sediment melt to the mantle source of the Gangdese magmatic rocks around 65 Ma, concurrent with the acceleration of India–Eurasia convergence. Numerical experiments suggest that subduction of sediments more than 1 km thick covering an approximately 1,000-km-wide ocean basin abutting the northern Indian passive margin starting from 65 Ma could have spurred the increased convergence rate and further led to significant crustal extension, consistent with empirical observations. Our study implies that the acceleration of India–Eurasia convergence marks the arrival of passive-margin-derived sediments, constraining the initial India–Eurasia collision to be around 60 Ma. It further suggests that temporary accelerations in subduction rates might be a common feature at the final stage of continental assembly.

The marked increase in the convergence rate between India and Eurasia, from approximately 8 cm yr⁻¹ to nearly 18 cm yr⁻¹ around 65 million years ago (Ma) (Fig. 1c), stands as one of the most thoroughly documented plate reorganization events in the Phanerozoic^{1–3,5–7,12}. Deciphering this underlying mechanism has important implications for understanding the driving and resisting forces of plate tectonics. Earlier studies have attributed this rapid increase in the convergence rate to either the arrival of the Reunion plume head^{4,6} or the development of a double-subduction system⁵. However, these theories have faced challenges from numerical models that demonstrate limited plate acceleration post-plume impingement⁶ and from uncertainties surrounding the plate history before the India–Eurasia collision^{5,13–16}. A largely overlooked parameter that may control plate speed is the rheological properties of the plate interface^{17–20}. Laboratory experiments have shown that sediments are intrinsically weaker and have a lower friction coefficient and higher pore fluid pressures than the mafic rocks that comprise the oceanic crust, leading to the speculation that sediment subduction may lubricate the plate interface and further cause the speed-up of plate convergence^{17,21–23}. However, there have been numerical models suggesting deceleration of convergence following sediment subduction owing to its intrinsic buoyancy²⁴. Additionally, it is unclear whether there was enough sediment subduction during the speed-up of the Indian plate and where those sediments came from. These contrasting ideas and doubts have obscured the effect of sediments on subduction dynamics.

Arc magmas at convergent margins serve as an important avenue for assessing the source and volume of subducted sediments, and they provide a unique opportunity to study the geodynamic effects of sediment subduction in the geological past. Here we perform geochemical analysis on the Late Cretaceous–Early Cenozoic magmatic rocks of the Gangdese arc to constrain the volume changes of subducted sediments, and we further combine numerical modelling and tectonic evolution to investigate the role of sediment subduction in controlling the India–Eurasia convergence. We propose a scenario where the large-scale erosion of the Indian passive margin produced large amounts of sediments that deposited on the Neo-Tethys Oceanic plate whose subduction caused the acceleration of India–Eurasia convergence and synchronous crustal extension in the upper plate. This scenario is consistent with multiple lines of observations and has important implications for the initial India–Eurasia collision.

Petrogenesis of Gangdese magmatic rocks

The Gangdese arc in southern Himalayan–Tibetan records the magmatism generated by the northward subduction of the Neo-Tethys Ocean and the subsequent India–Eurasia collision (Fig. 1a). It is composed of volcanic rocks of the Lower Jurassic Yeba Group (190–174 Ma), Upper Jurassic–Upper Cretaceous Sangri Group (136–93 Ma) (ref. 25) and Cretaceous–Tertiary Linzizong Group²⁶, as well as extensive intrusive rocks mainly generated during the Jurassic–Early Eocene (198–43 Ma)

¹Department of Earth and Space Sciences, Southern University of Science and Technology, Shenzhen, China. ²Guangdong Provincial Key Laboratory of Geophysical High-resolution Imaging Technology, Southern University of Science and Technology, Shenzhen, China. ³Earth Observatory of Singapore, Nanyang Technological University, Singapore, Singapore. ⁴Asian School of the Environment, Nanyang Technological University, Singapore, Singapore. ⁵Key Laboratory of Orogenic Belt and Crustal Evolution, MOE; School of Earth and Space Sciences, Peking University, Beijing, China. ⁶School of Earth Sciences and Engineering, Nanjing University, Nanjing, China. ✉e-mail: hujs@sustech.edu.cn

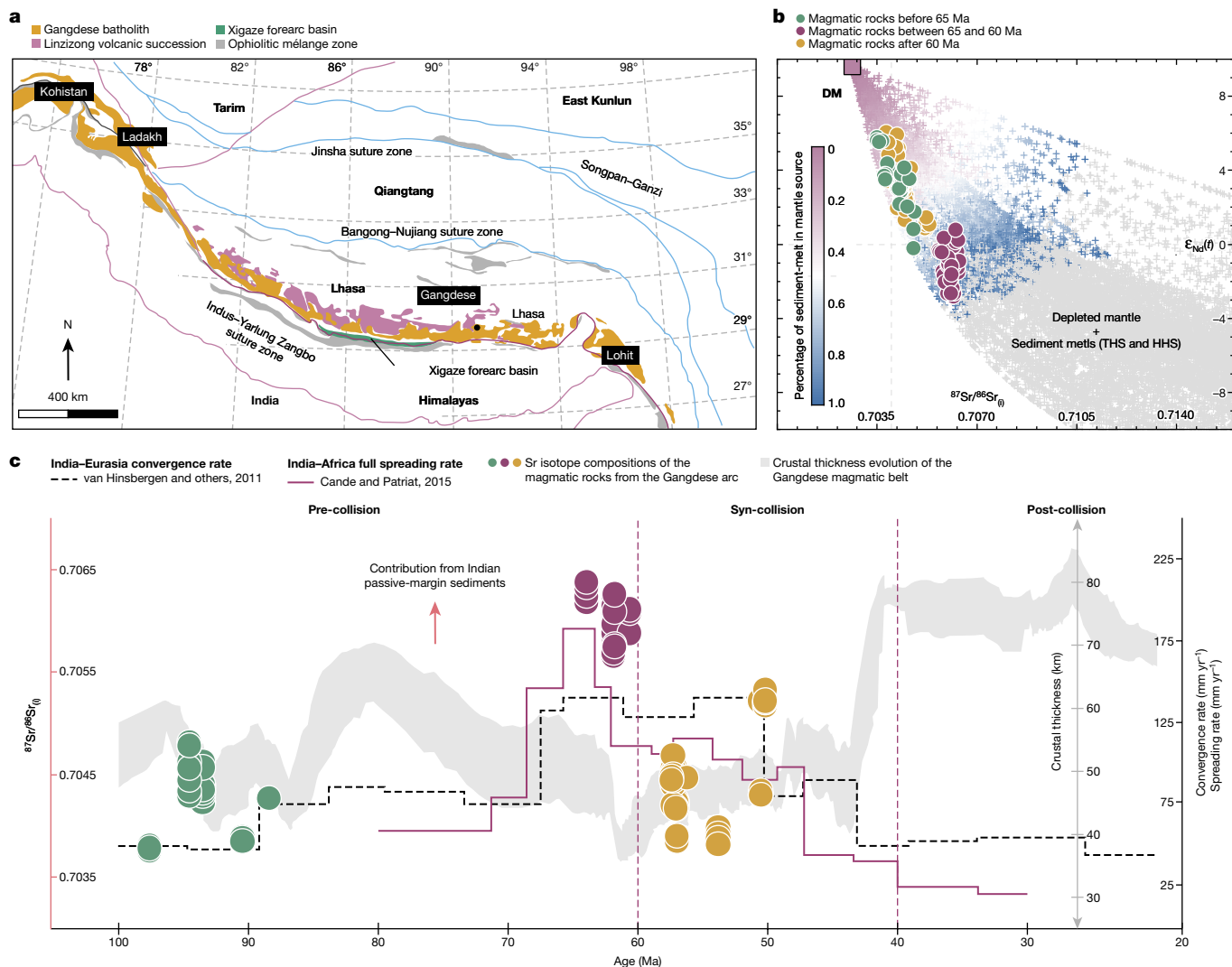


Fig. 1 | Variation of the India-Eurasia convergence rate and the isotope compositions of the magmatic rocks in the Gangdese arc. **a**, Tectonic framework of the Himalaya-Tibetan Plateau and the location of the Gangdese arc⁵⁷. **b**, Diagram of $\epsilon_{\text{Nd}}(t)$ versus $^{87}\text{Sr}/^{86}\text{Sr}_{(i)}$, showing the possible roles of Indian continental sediments (Tethys-Himalaya and High-Himalaya sediments) in the formation of the mantle source of the Gangdese Late Mesozoic-Early Cenozoic magmatic rocks during magmatic evolution (Methods). DM, depleted mantle; THS, Tethys-Himalaya sediments; HHS, High-Himalaya sediments. **c**, Variation

of Sr isotope composition, convergence rate and crustal thickness from 100 to 20 Ma. The coloured circles indicate the $^{87}\text{Sr}/^{86}\text{Sr}_{(i)}$ isotope ratios of magmatic rocks in the Gangdese arc (also see Extended Data Fig. 4). The grey shaded region represents the thickness of the Gangdese arc inferred from geochemical proxies (such as Sr/Y or La/Yb of whole rock and Eu/Eu* of zircons)⁴⁹. Dashed and solid lines show reconstructions of the India-Eurasia convergence rate and the India-Africa full-spreading rate (mm yr⁻¹) (refs. 2,6), respectively. **a**, Figure adapted with permission from ref. 57, Springer Nature Limited.

(ref. 27). To explore the link between the geochemical characteristics of these magmatic rocks and the subduction dynamics during the India-Eurasia convergence, we compiled whole-rock elemental and Sr-Nd isotopic data for magmatic rocks from approximately 100 to approximately 50 Ma in the southern part of the Gangdese arc and discuss their petrogenesis (Fig. 1b, Extended Data Figs. 1-4 and Supplementary Table 1).

In the primitive mantle-normalized trace element diagrams (Extended Data Fig. 2), most samples show variable enrichment in large ion lithophile elements (such as Ba, K and Sr) and light rare earth elements, and they exhibit depletions in high field strength elements (such as Nb, Ta and Ti), as observed in most arc magmas worldwide²⁸. However, the pre-65 Ma and post-60 Ma magmatic rocks generally show depleted Sr-Nd isotope compositions ($^{87}\text{Sr}/^{86}\text{Sr}_{(i)} < 0.7055$ and $\epsilon_{\text{Nd}}(t) > 0$; Fig. 1b), but samples between 65 and 60 Ma mostly display moderately enriched isotopic features ($^{87}\text{Sr}/^{86}\text{Sr}_{(i)} > 0.7055$ and $\epsilon_{\text{Nd}}(t) < 0$; Fig. 1b). The variable geochemical compositions could be attributed to shallow-level crustal processes (such as crustal

contamination) or heterogeneous mantle sources metasomatized by different components²⁸.

We examine the possible effects of the assimilation and crystal fractionation process on whole-rock geochemical composition (Extended Data Figs. 3 and 4). The depletion of MgO, Ni and Cr in most samples suggests that they are not in equilibrium with mantle peridotites and may have experienced fractional crystallization of olivine ± pyroxenes ± amphibole ± garnet from parental magma^{29,30}, which can lower magma Lu and Yb concentrations, for example. However, there are no correlations between the concentrations of trace elements (including Ba, Th, La, Yb, Lu and Hf) and SiO₂ contents within the individual groups (Extended Data Fig. 3), which indicates that the variations in these trace element concentrations do not result from fractional crystallization of a homogeneous primitive arc melt³¹. We suggest that the effect of crustal assimilation and magma mixing is also minor, as there is no negative or positive covariation patterns between whole-rock $^{87}\text{Sr}/^{86}\text{Sr}_{(i)}$, $\epsilon_{\text{Nd}}(t)$ values and SiO₂ contents (Extended Data Fig. 4). Additionally, geochemically inferred crustal thickness does not correlate with the

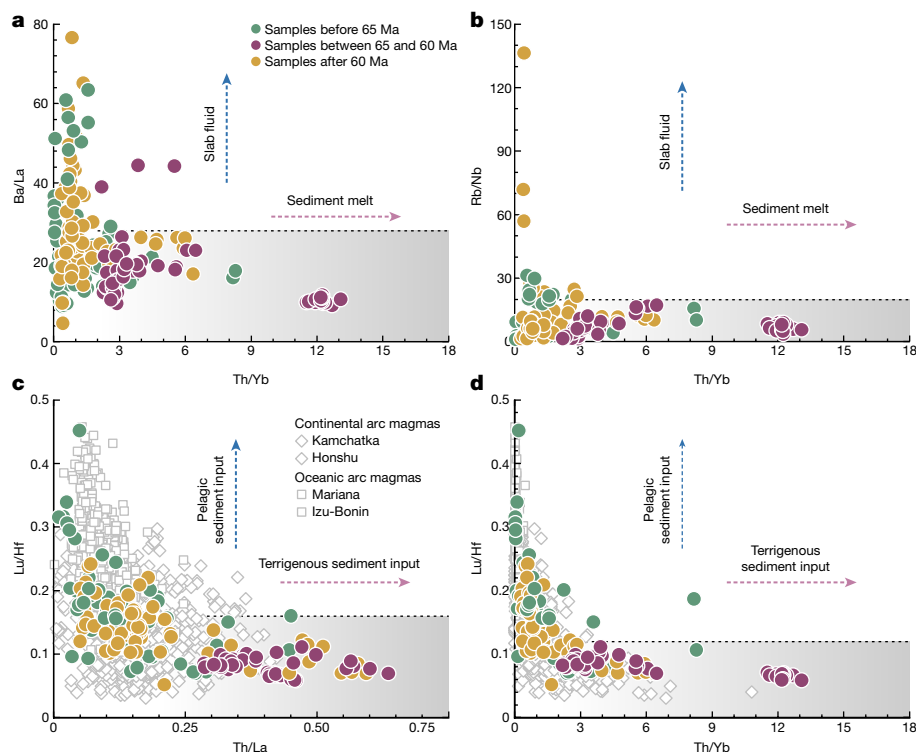


Fig. 2 | Trace element constraints on the metasomatic agents in mantle source. **a, b**, Diagrams showing the possible enriched components in the mantle source of the Late Cretaceous–Early Cenozoic magmatic rocks of the Gangdese arc, Ba/La versus Th/Yb (**a**) and Rb/Nb versus Th/Yb (**b**) (also see Extended Data Figs. 2 and 3). **c, d**, Diagrams showing the possible contribution of subducted sediments in the mantle source of the Late Cretaceous–Early Cenozoic magmatic rocks of the Gangdese arc, Lu/Hf versus Th/La (**c**) and Lu/Hf versus Th/Yb (**d**). The directions of the arrows indicate that the magmatic

enrichment of the magmatic samples (Fig. 1c), and thus does not favour the effect of crustal contamination. The above analysis suggests a minor influence of shallow-level crustal processes on whole-rock trace elements and isotope compositions.

Therefore, the variably enriched features of the Late Cretaceous to Early Cenozoic magmatic rocks from the Gangdese are most likely to be inherited from their mantle sources that were variably metasomatized by recycled components (fluid released from dehydration of the slab and/or melt derived from the subducted sediments)³¹. Owing to the different mobility of the trace elements in fluid and melt, we can decipher the relative contribution of fluid and melt to a depleted mantle source²⁸. For the pre-65 Ma and post-60 Ma samples, their high Ba/La and Rb/Nb (Fig. 2a,b) ratios suggest a dominant contribution from a slab-fluid component, whereas the Palaeocene (65–60 Ma) igneous rocks display low Ba/La, Rb/Nb and high Th/Yb, Th/La ratios, which indicates a predominant role of sediment melt in their mantle sources^{32,33}.

Source and amount of subducted sediments

More detailed geochemical analysis suggests a dominant role of terrigenous sediments in the enrichment of the subarc mantle for the Palaeocene (65–60 Ma) samples (Fig. 2c,d). As a result of the ‘zircon effect’, terrigenous sediments such as turbidites have low Lu/Hf ratios because of the abundant detrital zircons that have enriched Hf, whereas pelagic red clays have high Lu/Hf ratios due to the lack of zircons and rare earth element precipitation from seawater³⁴. The high Th/La and Th/Yb and low Lu/Hf ratios of the Gangdese magmatic rocks, in particular for the samples of the Palaeocene (circa 65–60 Ma), suggest a

close affinity of these samples with continental arc mafic rocks (such as Kamchatka and Honshu arcs) that are derived from mantle wedges metasomatized by addition of predominantly terrigenous sediments (Fig. 2c,d).

We suggest that these terrigenous sediments are unlikely to be sourced from the southern margin of Eurasia. The southern Eurasia, that is, the Lhasa Terrane, includes a central Precambrian microcontinent (Central Lhasa Terrane) and two surrounding juvenile Phanerozoic crustal blocks (Southern and Northern Lhasa Terrane)³⁵. The southern Lhasa Terrane should be juvenile and isotopically depleted because: (1) the Hf isotope mapping indicates that the Gangdese arc has large positive zircon $\varepsilon_{\text{Hf}}(t)$ values and young model ages³⁵; (2) granitic rocks formed between 103 and 85 Ma show depleted Sr–Nd isotopic compositions, which suggests a newly underplated, mafic lower crust^{36,37}; and (3) no ancient zircons have been reported in Cenozoic magmatic rocks. As weathering and erosion mainly affected the southern Lhasa Terrane³⁸, the resulting terrigenous sediments should not have the enriched isotopic leverage in contrast with the samples between 65 and 60 Ma. A natural explanation for the source of these terrigenous sediments is the large-scale erosion of the northern Indian passive margin. The Sr–Nd isotopic array of the Palaeocene samples toward Tethyan Himalaya sediment-derived components indicates the involvement of sediments in their origin (Fig. 1b). Previous studies show that it is feasible to estimate the proportion of subducted sediments by the whole-rock Sr–Nd isotope data^{32,33} (Methods). The modelling results demonstrate that the mantle source for the majority of Gangdese arc magmatic rocks was enriched by a variable proportion of melt (approximately 0.2–0.5% for pre-65 Ma samples and approximately 0.8–1.0% for samples between 65 and 60 Ma) derived from the subducted

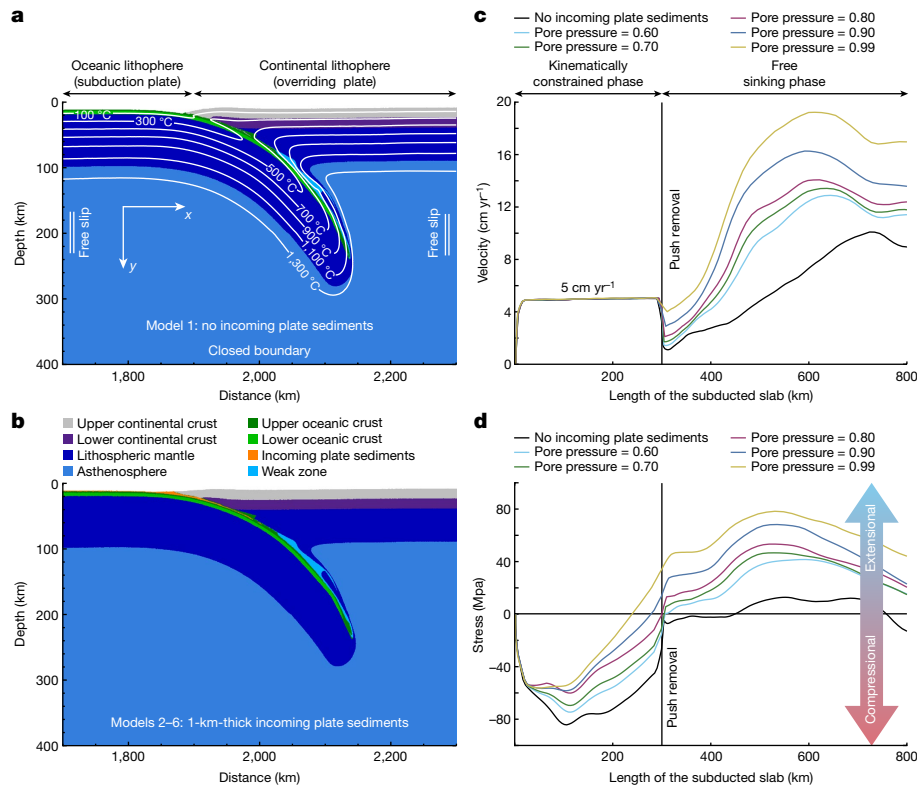


Fig. 3 | Results of numerical simulation. **a, b**, Model set-up of the zoomed-in region near the subduction zone. Model 1 has no incoming plate sediments (**a**). Models 2–6 have 1-km-thick incoming plate sediments with pore pressure increasing from 0.60 to 0.99, respectively (**b**). **c**, The relationship between subducting velocity and subducted slab length. **d**, The relationship between

overriding plate stress and slab length. The solid lines of different colours represent different models. The overriding plate stress is measured by computing the mean horizontal normal stress within the lithosphere at 300 km away from the trench. See details in the text.

sediments (Fig. 1b). It is worth noting that choosing different parameters may result in different mixing ratios. However, no matter what parameters we choose for the calculation, the proportion of the sediment melt in the mantle sources between 65 and 60 Ma was roughly 2–4 times that before 65 Ma.

Effects of sediment subduction

We designed a series of two-dimensional geodynamic models to investigate the effect of sediment subduction (Fig. 3), using the continuum, visco-elasto-plastic, seismo-thermo-mechanical version^{39,40} of I2ELVIS⁴¹. The code implements an implicit conservative finite difference scheme on a fully staggered Eulerian grid in combination with a Lagrangian marker-in-cell technique (Extended Data Fig. 5). The initial stage involved pushing an oceanic plate beneath a continental plate at a velocity of 5 cm yr⁻¹ for 6 Myr to establish the initial slab. The pushing force was then removed, and the system was left to evolve self-consistently. To investigate how sediments influence subduction, we varied: (1) the thickness of the incoming plate sediments from 0 km (no sediments: model 1) to 1 km (models 2–6; see detailed discussion about the thickness of the incoming plate sediments in Methods); and (2) the pore pressure of the incoming plate sediments from 0.60 to 0.99. Following earlier modelling approaches⁴², we used the flow law of wet quartzite for the upper oceanic crust, owing to the absence of experimental data for the flow law of hydrated basalt. To make the oceanic crust mechanically stronger than sediments, we set the pore pressure of the oceanic crust to be 0.60, which was lower than the subducting sediments; and we set the minimum dislocation-creep viscosity of the oceanic crust to be 1.0×10^{20} Pa s, which was two orders of magnitude higher than that for sediments, consistent with field and

experimental estimates¹⁷. More details of model set-up are described in Methods.

During the stage of free subduction, the incoming plate sediments served as the decoupling layer between the subducting and overriding plates in models 2–6. By contrast, for model 1, the decoupling zone occurred within the upper oceanic crust owing to the absence of incoming plate sediments (Extended Data Fig. 6). Before the subducting plate approached the bottom boundary, the subducting velocity increased because of the increase in slab pull and decrease in the integrated shear resistance along the plate interface. Our results show that sediment subduction can promote plate velocity (Fig. 3c and Extended Data Fig. 6). For model 1 (no incoming plate sediments), the largest subducting velocity was 10 cm yr⁻¹ before the subducting plate approached the bottom boundary. For model 2 (1 km incoming plate sediments with pore pressure 0.60), the maximum subducting velocity increased to a higher rate of 13 cm yr⁻¹. We further tested how the pore pressure of incoming plate sediments affects subducting velocity. The comparison of models 2–6 shows that an increase of pore pressure from 0.60 to 0.99 resulted in a higher subducting velocity from 13 to 19 cm yr⁻¹. This is because a higher pore pressure reduces the effective normal stress, leading to a lower yield stress and thus a lower effective viscosity along the plate interface.

Our model unveils intriguing dynamics in the relationship between the thickness and pore pressure of incoming plate sediments and the stress state of the overriding plate. By integrating the horizontal stress vertically within the overriding plate at a distance of 300 km from the trench, we could capture a snapshot of the overall stress of the overriding plate (Fig. 3d). Models with 1 km of incoming plate sediments (models 2–6) exhibited a more pronounced extensional stress response compared with model 1, which had no incoming plate sediments

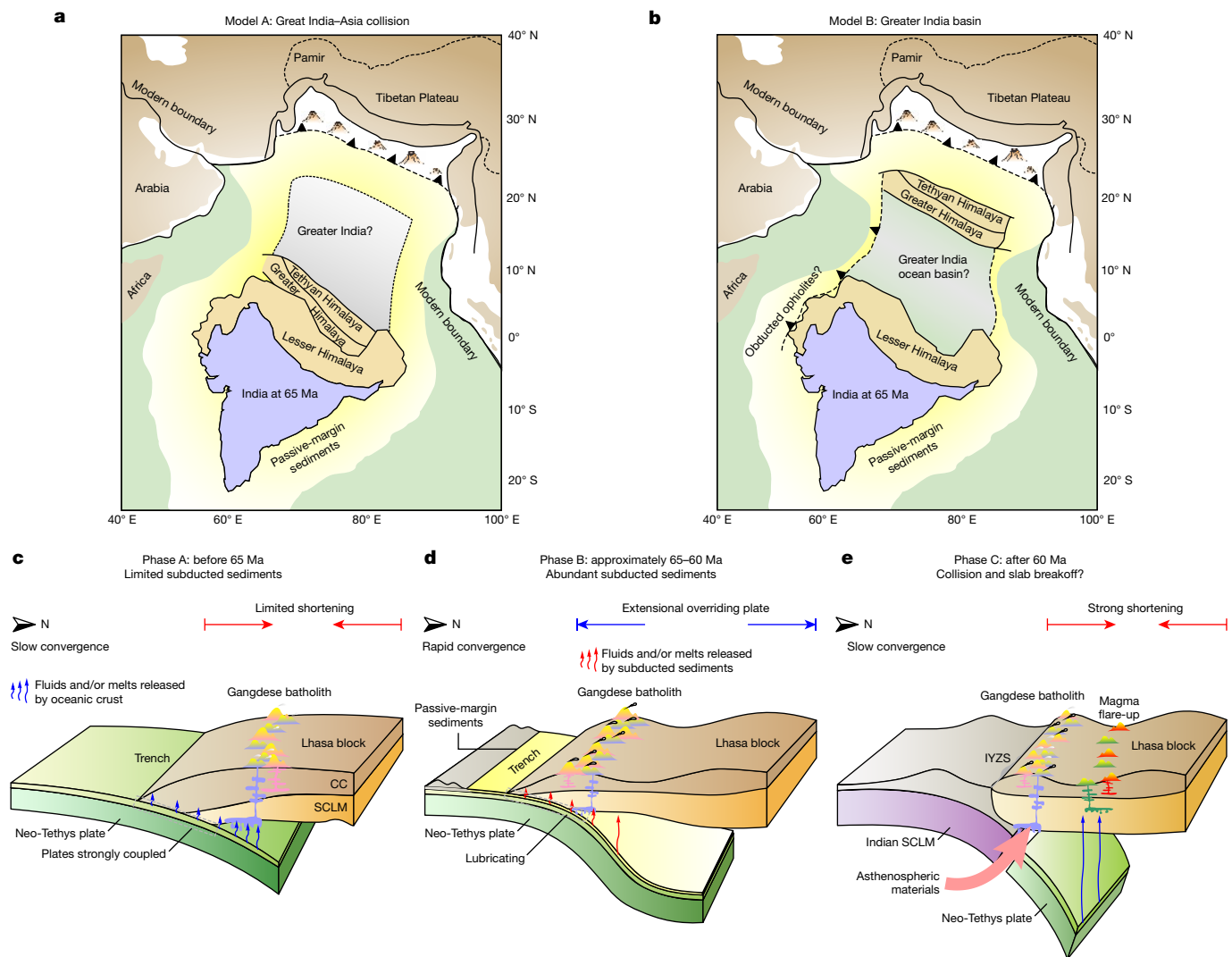


Fig. 4 | Two scenarios proposed for the Indo-Eurasian convergence. **a**, Model A: the Great Indian continent model⁵³ where the long-term large-scale erosion of the passive margin produced large amounts of sediments whose subduction led to the acceleration of India-Eurasia convergence at 65 Ma. **b**, Model B: the Great Indian Basin model^{14,53}; same as in model A, except that a pull-apart basin may have developed within the Indian continent before the subduction of the northern passive margin. Schematic showing three phases during the convergence between India and Eurasia. **c**, The first phase of convergence that was accompanied by limited shortening due to normal plate coupling. This had been operating since Late Cretaceous following the initial subduction of the Neo-Tethys Oceanic plate that was covered by limited pelagic sediments.

d, The second phase of convergence that was accompanied by strong extension of the overriding plate and rapid plate convergence due to the lubricating effect of the subducted sediments. This occurred during the Late Cretaceous to Early Cenozoic and was caused by subduction of thick terrigenous sediments derived from the northern Indian passive margin. **e**, The third phase due to the initial collision between India and Eurasia followed by slab breakoff. The velocity of the subducting plate would have decreased significantly due to the loss of slab pull. This phase of convergence was accompanied by strong shortening due to enhanced plate coupling. CC, continental crust; SCLM, subcontinental lithospheric mantle. **a, b**, Figures adapted with permission from ref. 58, *The American Journal of Science*.

(Fig. 3d and Extended Data Fig. 7). Remarkably, we observed that increased pore pressure of incoming plate sediments amplified this stress within the overriding plate (Fig. 3d). This finding is consistent with the understanding that higher pore pressure reduces the effective normal stress, leading to a lower effective friction along the plate interface, thereby weakening plate coupling and consequently diminishing the compressional stress in the overriding plate.

Implications for India-Eurasia convergence

Combining the geochemical analysis and numerical modelling, we suggest that the accelerated India-Eurasia convergence around 65 Ma was likely to have been caused by the increased terrigenous sediment subduction derived from the northern Indian passive margin. Sedimentological studies suggest that long-term large-scale erosion of

the passive margin can produce large amounts of sediments that can be transported to the ocean basin and cover a zone approximately 600–2,000 km wide⁴³ (see discussion in Methods). The continental slope and rise north to the Indian passive margin facilitated the transport of the sediments through gravity collapse and abyssal fans. Modern records of geophysical observations have also revealed thick sediment-covered zones (approximately 600–2,000 km wide and 1–10 km thick) in many other passive margins including those on the two sides of the Atlantic Ocean⁴⁴ (Extended Data Fig. 8). Those sediments have low Lu/Hf ratios due to the high zircon content, which is consistent with the geochemical characteristics of the Palaeocene (approximately 65–60 Ma) Gangdese magmatic rocks⁴⁵ (Fig. 2c,d). Interestingly, the acceleration of the Indian subduction rate around 65 Ma as constrained by the full-spreading rates along the India-Africa and India-Antarctic ridges seemed to last only about 5–10 Myr

(ref. 4) (Fig. 1c). This short duration is consistent with the typical width of the sediment-covered zone abutting passive margins assuming a convergence rate of around 18 cm yr⁻¹.

There have been numerical studies that suggest subduction of sediments leads to deceleration of convergence²⁴. This is because, in their models, an accretionary wedge was imposed, which has the same rheological properties (including the flow law and the pore pressure) as the incoming plate sediments; the upper oceanic crust has the same creep law as the sediments, although the pore pressure is lower than the sediments. As a result, the subduction channel is sufficiently weakened even without incoming plate sediments. In this case, the increase in sediment subduction leads to an increase in slab buoyancy, which causes the decrease in subducting velocity. We suggest that this accretionary wedge may not exist if an erosive boundary develops when limited incoming plate sediments subduct⁴⁶. Additionally, if more incoming plate sediments subduct, more fluids will be transported downward and be trapped in the subduction channel, introducing a higher pore pressure in the subduction channel than in the accretionary wedge^{47,48}. Our results suggest that when a subduction channel that is weaker than the surrounding rocks owing to sediment subduction is considered, the rheological effect outweighs the buoyancy effect, leading to an increase in subducting velocity (Fig. 3b).

Except for the accelerated convergence, our models also show reduced compressional stress in the overriding plate with increased sediment subduction. This may explain the crustal thinning event in southern Tibet. Geochemical analysis that applied Sr/Y and La/Yb ratios of whole-rock and Eu/Eu* of zircons indicates that significant thinning of crustal thickness in southern Tibet occurred at 65 Ma (refs. 49–51). The intense east–west trending veins at different locations (fore-arc, intra-arc and back-arc) in the Gangdese arc belt implied that the thinning of the crust was caused by extension rather than delamination⁵². The thinning of the arc crust facilitated the decompression melting of the magma, resulting in the mafic gabbro in the fore-arc and bimodal complex intrusion in the back-arc⁵². This is consistent with the reduced compressional stress in the overriding plate due to increased sediment subduction as suggested by our geodynamic models (Fig. 3d).

Two alternative mechanisms have been proposed to account for the accelerated India–Eurasia convergence at 65 Ma, including the plume push^{4,6} and the double-subduction hypotheses⁵. Although plume push helps in the acceleration of India–Eurasia convergence, it is not likely to be the dominant mechanism. There have been two episodes (at approximately 90 and 65 Ma) of convergence acceleration between India and Eurasia. Both followed the arrival of a mantle plume⁴. However, the increase of convergence rate at 65 Ma is more significant than the approximately 90 Ma event and much larger than can be explained by the arrival of a single plume head based on three-dimensional numerical models⁶. This suggests that other mechanisms are required to explain the 65 Ma convergence acceleration. In addition, if the push of the mantle plume strongly accelerated the convergence, the southern edge of Eurasia is likely to have experienced a phase of compression, which contradicts the thinning of the crust in southern Tibet around 65 Ma (refs. 49–51) (Fig. 1c). Although the development of two parallel northward dipping subduction zones might have created a significant increase in plate convergence rate between 80 and 65 Ma (ref. 5), there is a lack of geological evidence to support this scenario.

Our models also have important implications on the mode and timing of the initial India–Eurasia collision. Multiple models of India–Eurasia convergence have been proposed, including the Great Indian Continent⁵³, the Great Indian Basin¹⁴ and the double-subduction models¹¹, leading to severe debates on the timing of the initial collision^{15,54,55}. Our model implies that the initial collision between India and Eurasia occurred soon after the sediment-covered zone abutting the Indian continent was consumed by the convergent margin, which gives a collision age around 60 Ma (Fig. 4). This is consistent with the

abrupt change in sediment provenance recorded in trench settings, which dates the initial collision in the central-eastern Himalaya to be the middle Palaeocene (61–59 Ma) (refs. 54,56). In terms of the modes of the initial collision, our model is consistent with both the Great Indian Continent and the Great Indian Basin models (Fig. 4a,b). It is possible that a pull-apart basin had developed within the Indian continent before the subduction of the sediment-covered zone, as long as the spreading centre had frozen by then so that the stress in the northern subcontinent could be transmitted to the southern subcontinent.

In summary, we suggest that the acceleration of India–Eurasia convergence at 65 Ma is likely to have been caused by subduction of the sediment-covered ocean basin abutting the northern Indian passive margin (Fig. 4d). Although plume push and double subduction could potentially have accelerated the India–Eurasia convergence, we emphasize that a reduced plate coupling due to sediment subduction derived from the passive margin is required to account for the geochemical signature of the magmatic arc and the complex array of geological processes associated with convergence rate, stress state and crustal evolution of the upper plate. The proposed scenario also suggests that the acceleration of India–Eurasia convergence marks the final closure of the Neo-Tethys Ocean, constraining the initial India–Eurasia collision to have occurred around 60 Ma. We further propose temporary acceleration of convergence due to passive-margin-sourced sediment subduction, which may have been a common phenomenon during continental assembly. This should catalyse new research inquiries on similar geodynamic scenarios globally.

Online content

Any methods, additional references, Nature Portfolio reporting summaries, source data, extended data, supplementary information, acknowledgements, peer review information; details of author contributions and competing interests; and statements of data and code availability are available at <https://doi.org/10.1038/s41586-024-08069-6>.

1. Patriat, P. & Achache, J. India–Eurasia collision chronology has implications for crustal shortening and driving mechanism of plates. *Nature* **311**, 615–621 (1984).
2. Cande, S. C. & Patriat, P. The anticorrelated velocities of Africa and India in the Late Cretaceous and early Cenozoic. *Geophys. J. Int.* **200**, 227–243 (2015).
3. Copley, A., Avouac, J. P. & Royer, J. Y. India–Asia collision and the Cenozoic slowdown of the Indian plate: implications for the forces driving plate motions. *J. Geophys. Res. Solid Earth* **115**, B03410 (2010).
4. Cande, S. C. & Stegman, D. R. Indian and African plate motions driven by the push force of the Réunion plume head. *Nature* **475**, 47–52 (2011).
5. Jagoutz, O., Royden, L., Holt, A. F. & Becker, T. W. Anomalously fast convergence of India and Eurasia caused by double subduction. *Nat. Geosci.* **8**, 475–478 (2015).
6. Van Hinsbergen, D. J. J., Steinberger, B., Doubrovine, P. V. & Gassmüller, R. Acceleration and deceleration of India–Asia convergence since the Cretaceous: roles of mantle plumes and continental collision. *J. Geophys. Res. Solid Earth* **116**, B06101 (2011).
7. Pusok, A. E. & Stegman, D. R. The convergence history of India–Eurasia records multiple subduction dynamics processes. *Sci. Adv.* **6**, eaaz8681 (2020).
8. Wan, B. et al. Cyclical one-way continental rupture–drift in the Tethyan evolution: subduction-driven plate tectonics. *Sci. China–Earth Sci.* **62**, 2005–2016 (2019).
9. Forsyth, D. & Uyeda, S. On the relative importance of the driving forces of plate motion. *Geophys. J. Int.* **43**, 163–200 (1975).
10. Holt, A. F., Royden, L. H. & Becker, T. W. The dynamics of double slab subduction. *Geophys. J. Int.* **209**, 250–265 (2017).
11. Pusok, A. E. & Stegman, D. R. Formation and stability of same-dip double subduction systems. *J. Geophys. Res. Solid Earth* **124**, 7387–7412 (2019).
12. Cande, S. C., Patriat, P. & Dymment, J. Motion between the Indian, Antarctic and African plates in the early Cenozoic: Indian Ocean Plate motions. *Geophys. J. Int.* **183**, 127–149 (2010).
13. Ingalls, M., Rowley, D. B., Currie, B. & Colman, A. S. Large-scale subduction of continental crust implied by India–Asia mass-balance calculation. *Nat. Geosci.* **9**, 848–853 (2016).
14. Van Hinsbergen, D. J. J. et al. Greater India Basin hypothesis and a two-stage Cenozoic collision between India and Asia. *Proc. Natl Acad. Sci. USA* **109**, 7659–7664 (2012).
15. DeCelles, P. G., Kapp, P., Gehrels, G. E. & Ding, L. Paleocene–Eocene foreland basin evolution in the Himalaya of southern Tibet and Nepal: implications for the age of initial India–Asia collision. *Tectonics* **33**, 824–849 (2014).
16. Yuan, J. et al. Rapid drift of the Tethyan Himalaya terrane before two-stage India–Asia collision. *Nat. Sci. Rev.* **8**, nwaaf173 (2020).
17. Behr, W. M. & Becker, T. W. Sediment control on subduction plate speeds. *Earth Planet. Sci. Lett.* **502**, 166–173 (2018).

18. Hu, J., Liu, L. & Gurnis, M. Southward expanding plate coupling due to variation in sediment subduction as a cause of Andean growth. *Nat. Commun.* **12**, 7271 (2021).
19. Sobolev, S. V. & Brown, M. Surface erosion events controlled the evolution of plate tectonics on Earth. *Nature* **570**, 52–57 (2019).
20. Sobolev, S. V. & Babeyko, A. Y. What drives orogeny in the Andes? *Geology* **33**, 617–620 (2005).
21. Tobin, H. J. & Saffer, D. M. Elevated fluid pressure and extreme mechanical weakness of a plate boundary thrust, Nankai Trough subduction zone. *Geology* **37**, 679–682 (2009).
22. Kopf, A. & Brown, K. M. Friction experiments on saturated sediments and their implications for the stress state of the Nankai and Barbados subduction thrusts. *Mar. Geol.* **202**, 193–210 (2003).
23. Bangs, N. L. B. et al. Broad, weak regions of the Nankai Megathrust and implications for shallow coseismic slip. *Earth Planet. Sci. Lett.* **284**, 44–49 (2009).
24. Brizzi, S. et al. The role of sediment accretion and buoyancy on subduction dynamics and geometry. *Geophys. Res. Lett.* **48**, e2021GL096266 (2021).
25. Zhu, D. C. et al. Early Cretaceous subduction-related adakite-like rocks of the Gangdese Belt, southern Tibet: products of slab melting and subsequent melt–peridotite interaction? *J. Asian Earth Sci.* **34**, 298–309 (2009).
26. Mo, X. X. et al. Mantle contributions to crustal thickening during continental collision: evidence from Cenozoic igneous rocks in southern Tibet. *Lithos* **96**, 225–242 (2007).
27. Zhu, D. C., Wang, Q., Chung, S. L., Cawood, P. A. & Zhao, Z. D. Gangdese magmatism in southern Tibet and India–Asia convergence since 120 Ma. *Geol. Soc. Spec. Publ.* **483**, 583–604 (2019).
28. Pearce, J. A. & Peate, D. W. Tectonic implications of the composition of volcanic ARC magmas. *Annu. Rev. Earth Planet. Sci.* **23**, 251–285 (1995).
29. Schmidt, M. W. & Jagoutz, O. The global systematics of primitive arc melts. *Geochem. Geophys. Geosyst.* **18**, 2817–2854 (2017).
30. Müntener, O. & Ulmer, P. Arc crust formation and differentiation constrained by experimental petrology. *Am. J. Sci.* **318**, 64–89 (2018).
31. Chen, L., Zheng, Y. F., Zhao, Z. F., An, W. & Hu, X. M. Continental crust recycling in ancient oceanic subduction zone: geochemical insights from arc basaltic to andesitic rocks and paleo-trench sediments in southern Tibet. *Lithos* **414–415**, 106619 (2022).
32. Zhao, L., Guo, F., Fan, W. M. & Huang, M. Roles of subducted pelagic and terrigenous sediments in Early Jurassic mafic magmatism in NE China: constraints on the architecture of paleo-Pacific subduction zone. *J. Geophys. Res. Solid Earth* **124**, 2525–2550 (2019).
33. Guo, F. et al. Magmatic responses to Cretaceous subduction and tearing of the paleo-Pacific Plate in SE China: an overview. *Earth Sci. Rev.* **212**, 103448 (2021).
34. Patchett, P. J., White, W. M., Feldmann, H., Kielinczuk, S. & Hofmann, A. W. Hafnium/rare earth element fractionation in the sedimentary system and crustal recycling into the Earth's mantle. *Earth Planet. Sci. Lett.* **69**, 365–378 (1984).
35. Hou, Z. et al. Lithospheric architecture of the Lhasa Terrane and its control on ore deposits in the Himalayan–Tibetan orogen. *Econ. Geol.* **110**, 1541–1575 (2015).
36. Wen, D. R. et al. Late Cretaceous Gangdese intrusions of adakitic geochemical characteristics, SE Tibet: petrogenesis and tectonic implications. *Lithos* **105**, 1–11 (2008).
37. Huang, T. Y. et al. Subduction erosion revealed by Late Mesozoic magmatism in the Gangdese arc, South Tibet. *Geophys. Res. Lett.* **49**, e2021GL097360 (2022).
38. Ding, L. et al. Timing and mechanisms of Tibetan Plateau uplift. *Nat. Rev. Earth Environ.* **3**, 652–667 (2022).
39. van Dinther, Y. et al. The seismic cycle at subduction thrusts: insights from seismo-thermo-mechanical models. *J. Geophys. Res. Solid Earth* **118**, 6183–6202 (2013).
40. Dal Zilio, L., Kissling, E., Gerya, T. & van Dinther, Y. Slab rollback orogeny model: a test of concept. *Geophys. Res. Lett.* **47**, e2020GL089917 (2020).
41. Gerya, T. V. & Yuen, D. A. Robust characteristics method for modelling multiphase visco-elasto-plastic thermo-mechanical problems. *Phys. Earth Planet. Inter.* **163**, 83–105 (2007).
42. Gerya, T. & Stöckhert, B. Two-dimensional numerical modeling of tectonic and metamorphic histories at active continental margins. *Int. J. Earth Sci. (Geol. Rundsch)* **95**, 250–274 (2006).
43. Heezen, B. C., Ericson, D. B. & Ewing, M. Further evidence for a turbidity current following the 1929 Grand Banks earthquake. *Deep Sea Res. (1953)* **1**, 193–202 (1954).
44. Straume, E. O. et al. GlobSed: updated total sediment thickness in the world's oceans. *Geochem. Geophys. Geosyst.* **20**, 1756–1772 (2019).
45. Plank, T. & Langmuir, C. H. The chemical composition of subducting sediment and its consequences for the crust and mantle. *Chem. Geol.* **145**, 325–394 (1998).
46. Pusok, A. E., Stegman, D. R. & Kerr, M. The effect of low-viscosity sediments on the dynamics and accretionary style of subduction margins. *Solid Earth* **13**, 1455–1473 (2022).
47. Sibson, R. H. Stress switching in subduction forearcs: implications for overpressure containment and strength cycling on megathrusts. *Tectonophysics* **600**, 142–152 (2013).
48. Faulkner, D. R. et al. A review of recent developments concerning the structure, mechanics and fluid flow properties of fault zones. *J. Struct. Geol.* **32**, 1557–1575 (2010).
49. Tang, M., Ji, W. Q., Chu, X., Wu, A. & Chen, C. Reconstructing crustal thickness evolution from europium anomalies in detrital zircons. *Geology* **49**, 76–80 (2020).
50. Hu, F. et al. Quantitatively tracking the elevation of the Tibetan Plateau since the Cretaceous: insights from whole-rock Sr/Y and La/Yb ratios. *Geophys. Res. Lett.* **47**, e2020GL089202 (2020).
51. Guo, P. & Yang, T. Quantifying continental crust thickness using the machine learning method. *J. Geophys. Res. Solid Earth* **128**, e2022JB025970 (2023).
52. Zhao, Z. D. et al. Distribution and its significance of dikes in southern Tibetan Plateau. *Acta Petrol. Sin.* **37**, 3399–3412 (2021).
53. van Hinsbergen, D. J. J. et al. Restoration of Cenozoic deformation in Asia and the size of Greater India. *Tectonics* **30**, TC5003 (2011).
54. Hu, X. M., Garzanti, E., Moore, T. & Raffi, I. Direct stratigraphic dating of India–Asia collision onset at the Selandian (middle Paleocene, 59±1 Ma). *Geology* **43**, 859–862 (2015).
55. Orme, D. A., Carrapa, B. & Kapp, P. Sedimentology, provenance and geochronology of the upper Cretaceous–lower Eocene western Xigaze forearc basin, southern Tibet. *Basin Res.* **27**, 387–411 (2015).
56. An, W., Hu, X. M., Garzanti, E., Wang, J. G. & Liu, Q. New precise dating of the India–Asia collision in the Tibetan Himalaya at 61 Ma. *Geophys. Res. Lett.* **48**, e2020GL090641 (2021).
57. Zhu, D. C. et al. Interplay between oceanic subduction and continental collision in building continental crust. *Nat. Commun.* **13**, 7141 (2022).
58. Kapp, P. & DeCelles, P. G. Mesozoic–Cenozoic geological evolution of the Himalayan–Tibetan orogen and working tectonic hypotheses. *Am. J. Sci.* **319**, 159–254 (2019).

Publisher's note Springer Nature remains neutral with regard to jurisdictional claims in published maps and institutional affiliations.



Open Access This article is licensed under a Creative Commons Attribution-NonCommercial-NoDerivatives 4.0 International License, which permits any non-commercial use, sharing, distribution and reproduction in any medium or format, as long as you give appropriate credit to the original author(s) and the source, provide a link to the Creative Commons licence, and indicate if you modified the licensed material. You do not have permission under this licence to share adapted material derived from this article or parts of it. The images or other third party material in this article are included in the article's Creative Commons licence, unless indicated otherwise in a credit line to the material. If material is not included in the article's Creative Commons licence and your intended use is not permitted by statutory regulation or exceeds the permitted use, you will need to obtain permission directly from the copyright holder. To view a copy of this licence, visit <http://creativecommons.org/licenses/by-nc-nd/4.0/>.

© The Author(s) 2024

Methods

Selection of studied samples

This study included mafic to intermediate plutonic rocks that were produced by the magmatic flare-up event at circa 105–85 Ma and the post-collision event after 60 Ma in the southern part of the Gangdese arc. These rocks are dominated by diorite, gabbro, hornblende and norites with a minor amount of pseudoleucite phonolite and appinite-granite^{59–68}. These plutons occur subparallel to the India–Yarlung Zangbo suture zone (IYZSZ) along a narrow east–west strike belt. The samples included, from west to east: (1) circa 158 Ma diorite porphyry and 90 Ma gabbro diorite in the Dazhuka area (Xigaze)⁶¹; (2) circa 93 and 91 Ma gabbro in the Namling area⁶³; (3) circa 50 Ma appinite-granite suite in the Pengculin area⁶⁵; (4) circa 97 Ma gabbro and 51 Ma diorite in the Nyemo area⁶⁸; (5) a suite of early Cenozoic mafic rocks (circa 57 Ma) in the Dazi area⁶⁷; (6) circa 94 Ma diorite-gabbro suite in the Zhengga area⁶⁰; (7) circa 98 to approximately 88 Ma amphibole gabbro between Langxian and the Milin area from the eastern segment of the southern Lhasa Terrane⁶²; (8) circa 93 Ma norite and hypersthene-bearing hornblendites in the Milin area⁵⁹; (9) circa 64 Ma pseudoleucite phonolitic dike in the Rongniduo area from the central Lhasa Terrane⁶⁴; and (10) circa 50 Ma gabbroic rocks from the central and eastern Gangdese arc⁶⁶. Geochemically, these calc-alkaline rocks in the Gangdese arc are similar to plutonic rocks from the Cordilleran orogen along the western margin of the American continents above the eastern Pacific subduction zone, the typical products of continental arc magmatism. They generally show depleted Sr–Nd isotope compositions (Fig. 1).

In addition to the Late Cretaceous–Early Cenozoic plutonic rocks, we also selected volcanic rocks from the Gangdese arc, such as the Linzizong volcanic succession (LVS). The LVS, extending east–west for more than 1,000 km, is distributed extensively in the south Gangdese arc^{69,70}. It is considered to be a suite of so-called syn-collision genetic volcanic rocks, which were formed during the India–Asia collision from approximately 65 to approximately 40 Ma, indicating that a continuous volcanic activity lasted for approximately 25 Ma. On the other hand, the LVS can also be interpreted as resulting from Neo-Tethyan Ocean plate subduction beneath the Eurasian Andean-type continental margin if the India–Asia collision commenced later²⁶. So far, a relatively detailed study of the LVS rocks has been limited to the Linzhou and Numling Basins near Lhasa^{70–72}, readily subdivided into lower Dianzhong, middle Nianbo and upper Pana formations based on the eruption hiatuses^{70–72}. In this study, the representative basaltic and andesitic rocks were collected from the Dianzhong formation of the LVS in the Linzhou Basin, which is located in the northeastern part of the Gangdese arc^{69,70}. They generally show moderately enriched Sr–Nd isotope compositions (Fig. 1b).

Monte Carlo isotope mixing model

To quantify the amount of sediment-derived melt in the mantle sources of the Gangdese magmatic rocks, we developed a binary mixing simulation between depleted mantle⁷³ and melts derived from partial melting of Indian passive-margin sediments⁷⁴ (represented by Tethys–Himalaya and High-Himalaya sediments) (Extended Data Table 1). To better estimate the proportion of the sediment-derived melt in the mantle sources, we assumed that the elemental mobilities for Sr and Nd were 0.46 and 0.21 during the dehydration of sediments⁷⁵. The partition coefficients of Sr and Nd were assumed to be 0.001 and 0.05, respectively, during sediment melting^{33,76}. A moderate melting degree ($F = 0.5$) of the subducted sediments was assumed based on an experimental study⁷⁷. Batch melting mode⁷⁸ was used for the calculation of the elemental concentrations in the sediment-derived melt, following the equations below:

$$C_{x\text{-res}} = C_{x\text{-bulk}} \times (1 - M_x)$$
$$C_{x\text{-melt}} = C_{x\text{-res}} / [(1 - F) \times D_x + F]$$

where x is Sr or Nd, $C_{x\text{-bulk}}$ are the element concentrations of x for sediments listed in Extended Data Table 1, $C_{x\text{-res}}$ are the element concentrations of x after dehydration, $C_{x\text{-melt}}$ are the final element concentrations of x for sediment-derived melt in the mantle sources, M_x is the mobility of the element, D_x is the bulk partition coefficient, and F is the melting degree. The binary mixing simulation is calculated after Faure and Mensing (2004)⁷⁹:

$$C_x = C_{x\text{-melt}} \times f + C_m \times (1 - f)$$
$$R_x = R_{x\text{-melt}} \times f \times (C_{x\text{-melt}}/C_x) + R_m \times (1 - f) \times (C_m/C_x)$$

where C_x and R_x are element concentrations and isotopic ratios [$^{87}\text{Sr}/^{86}\text{Sr}_{(i)}$ and $\varepsilon_{\text{Nd}}(t)$] after mixing, respectively, C_m and R_m are element concentration and isotopic ratio of mantle-derived melt (Extended Data Table 1), $R_{x\text{-melt}}$ are isotopic ratios of sediment melt and f is the proportion of sediment-derived melt.

To explore the composition range of sediment under as many as possible scenarios, we randomly selected two sediments from the Tethys–Himalaya or High-Himalaya sediment database⁷⁴ and then mixed them in random proportions to make a new sediment–melt end-member. Finally, this new sediment melt was mixed with the mantle with a sediment proportion of 0–5%. A total of 30,000 sediment–melt–mantle mixtures were yielded using this method (Fig. 1b).

Numerical model set-up

We use the two-dimensional, continuum, visco-elasto-plastic, seismo-thermo-mechanical version³⁹ of the code I2ELVIS⁴¹, which implemented an implicit, conservative finite difference scheme on a fully staggered Eulerian grid in combination with a Lagrangian marker-in-cell technique. The code solves mass, momentum and energy conservation with visco-plastic rheology. Lagrangian markers advect physical properties (for example, viscosity, stress, plastic strain and temperature) according to the velocity field interpolated from the Eulerian grid⁴¹. The computational domain was $2,500 \times 1,200 \text{ km}^2$ ($1,891 \times 416$ nodes). The grid size was 500 m in the high-resolution area around the trench and increased to 10,000 m at the edges of the model (Extended Data Fig. 5). The method is provided in more detail by Brizzi et al.²⁴.

The model set-up was similar to that used by Brizzi et al.²⁴. It consisted of an oceanic lithosphere (2 km upper crust and 5 km lower crust) that subducted beneath the continental lithosphere. The oceanic lithosphere also included a sedimentary layer with thickness of 0 km (no sediments) or 1 km covering the oceanic crust. The sediment layer was designed to deliver a constant sediment flux to the subduction zone. The continental crust consisted of a 15.0-km-thick upper crust and a 15.0-km-thick lower crust. The lithological structure was resolved with approximately 33 million markers. The rheological properties of different compositions are listed in Extended Data Table 2.

A 12.5-km-thick layer of sticky air (viscosity of sticky air (η_{air}) = 10^{18} Pa s , density of sticky air (ρ_{air}) = 1 kg m^{-3}) mimics the effect of a free surface and enables the development of topography⁸⁰. Free slip boundary conditions were applied at the top and side boundaries of the model, and we imposed a closed boundary condition at the bottom boundary.

The initial thermal structure of the oceanic and continental lithosphere was calculated from the half-space cooling model⁸¹, assuming a thermal diffusivity of $10^{-6} \text{ m}^2 \text{ s}^{-1}$. An 80–40 Ma oceanic lithosphere (80 Ma for the left side and 40 Ma for the right side) was defined, which trailed an 80 Ma continental lithosphere that represented the Indian continent and subducted beneath a 40 Ma continental lithosphere that represented the southern margin of Eurasia. The thermal gradient of the asthenospheric mantle was adiabatic and set to be $0.5 \text{ }^\circ\text{C km}^{-1}$.

A 15° -dipping weak zone with low plastic strength (1 MPa) and wet olivine rheology was used to promote the initial subduction⁸². We imposed a constant velocity of 5 cm yr^{-1} within a small region of the subducting plate (Extended Data Fig. 5) until 300 km of the slab was subducted into the mantle, which corresponded to 6 Myr of subduction. After this

kinematically prescribed phase, the pushing velocity was removed and subduction was self-driven.

Thickness of the incoming plate sediments

Previous studies have indicated that there should be a relatively thick layer of terrigenous clastic sediments deposited on the northern margin of the Indian continent and possibly also on the Neo-Tethyan oceanic crust. First, during the Late Triassic period, evidence suggests the development of a significant submarine fan complex that spanned a broad region, including the distal Tethys Himalayan margin^{83,84}, which explains the fact that the age-equivalent strata in Tethyan Himalaya, Northwest Australia, Timor and West Sulawesi all contain abundant Permian–Triassic detrital zircons and exhibit similar sedimentary facies. The Langjiexue Group and Nieru Formation in the Kangma region of the eastern Tethyan Himalaya were likely to have been deposited as a distal part of this submarine fan complex, which can explain the source of the subducted sediments^{83,85}. Second, climate factors should have led to increased sediment supply to the Neo-Tethys Ocean plate abutting the Indian passive margin from surface erosion. As the Indian continent drifted northward from the southern hemisphere it passed through the equator. The warm climate of this region led to a high erosion rate of bedrock, contributing to the high sediment accumulation rates in low-topography regions. This was a favourable condition for the development of thicker sediments along the northern margin of the Indian continent and the abutting ocean basin⁸⁶. Third, passive-margin turbidite fans may indeed extend for several hundreds of kilometres into the ocean if associated with huge river systems draining vast continental interiors⁸⁷. Modern records of geophysical observations have also revealed thick sediment-covered zones (600–2,000 km wide and 1–10 km thick) in many other passive margins⁴⁴. To determine the distribution and thickness of sediments on the oceanic crust neighbouring the passive margin, we conducted a comparison of the global distribution of marine sediments, the age of the oceanic crust and the ocean–continent boundaries (Extended Data Fig. 8). Our findings indicate that there are significant amounts of sediments present on the oceanic crust adjacent to the passive margin on both sides of the Atlantic Ocean and Indian Ocean. The source area for these sediments was mainly the passive continental crust that was subjected to weathering and erosive effects. Sediment with a thickness greater than 1 km covers widths ranging from 600 to 2,000 km. These widths may vary depending on factors such as the topography and age of the oceanic crust. A natural inference from this is that, as an ancient passive margin, the Indian continent is expected to exhibit similar characteristics. In conclusion, despite the distal Tethys Himalayan margin being characterized by starved sedimentation throughout the Late Cretaceous⁵⁴, erosion did occur earlier, leading to the formation of sediments of considerable thickness.

In light of our discussions, we integrated a 1-km-thick layer of subducted sediments into our model. This integration was part of our endeavour to understand sediment accretion dynamics and changes in sediment properties during plate convergence. We found that a thickness of 1 km for sediments is adequate to decouple the converging plates¹⁸. At this specific thickness, the nature of subduction may be erosive or marginally accretionary, which implies that substantial amounts of sediments are unlikely to be trapped within the accretionary wedge. This finding also explains why sediments in the trench basin may not be preserved if the subduction velocity is excessively high⁸⁸. Indeed, the very limited number of small oceanic accretionary complexes along the Yarlung Zangbo suture zone in southern Tibet suggests that tectonic erosion was predominant at this active continental margin for the majority of the subduction period⁸⁹. In zones where tectonic erosion dominates, there is an absence of accretion, and all sediments along with material eroded from the overriding plate are incorporated into the subduction channel^{90,91}. This is also consistent with the results of our models (Extended Data Fig. 6). However, sediments on the continental

shelf might be preserved, as the sediments are expected to be thicker and continental collision slowed down the convergence.

Data availability

All data used in this study are from the published literature as referenced in Figs. 1 and 2 and Extended Data Figs. 1–4 (refs. 59–70). These data and the data generated by the numerical models are available at Dryad (<https://doi.org/10.5061/dryad.8kpr4xwr>)⁹². Source data are provided with this paper.

Code availability

The geodynamic modelling software I2ELVIS used for numerical experiments can be obtained from <https://doi.org/10.17605/OSF.IO/bnvth> and the MATLAB code for visualization is available at Dryad (<https://doi.org/10.5061/dryad.8kpr4xwr>)⁹².

59. Ma, L. et al. Early Late Cretaceous (ca. 93 Ma) norites and hornblendites in the Milin area, eastern Gangdese: lithosphere–asthenosphere interaction during slab roll-back and an insight into early Late Cretaceous (ca. 100–80 Ma) magmatic “flare-up” in southern Lhasa (Tibet). *Lithos* **172–173**, 17–30 (2013).
60. Ma, L. et al. Late Cretaceous crustal growth in the Gangdese area, southern Tibet: petrological and Sr–Nd–Hf–O isotopic evidence from Zhengga diorite–gabbro. *Chem. Geol.* **349–350**, 54–70 (2013).
61. Meng, Y. K. et al. Late Mesozoic diorites of the middle Gangdese magmatic belt of southern Tibet: new insights from SHRIMP U–Pb dating and Sr–Nd–Hf–O isotopes. *Lithos* **404–405**, 106420 (2021).
62. Guan, Q. et al. Zircon U–Pb chronology, geochemistry of the Late Cretaceous mafic magmatism in the southern Lhasa Terrane and its implications. *Acta Petrol. Sin.* **27**, 2083–2094 (2011).
63. Tang, Y. et al. Geochemistry and petrogenesis of Late Cretaceous Namling gabbro and dykes in Gangdese batholith, Tibet. *Acta Petrol. Sin.* **35**, 387–404 (2019).
64. Qi, Y. et al. Cenozoic mantle composition evolution of southern Tibet indicated by Paleocene (–64 Ma) pseudoleucite phonolitic rocks in central Lhasa terrane. *Lithos* **302–303**, 178–188 (2018).
65. Huang, F. et al. Fluid flux in the lithosphere beneath southern Tibet during Neo-Tethyan slab breakoff: evidence from an appinite–granite suite. *Lithos* **344–345**, 324–338 (2019).
66. Wang, Y. F. et al. Along-arc variations in isotope and trace element compositions of Paleogene gabbroic rocks in the Gangdese batholith, southern Tibet. *Lithos* **324–325**, 877–892 (2019).
67. Huang, F., Rooney, T. O., Xu, J. F. & Zeng, Y. C. Magmatic record of continuous Neo-Tethyan subduction after initial India–Asia collision in the central part of southern Tibet. *GSA Bull.* **133**, 1600–1612 (2020).
68. Lei, M., Chen, J. L., Huang, F. & Liu, Y. X. Mantle wedge enrichment beneath southern Tibet during the late stage (100–45 Ma) of oceanic subduction: geochemical constraints from mantle-derived intrusions. *Lithos* **406–407**, 106505 (2021).
69. Yan, H. Y. et al. Arc andesitic rocks derived from partial melts of mélange diapir in subduction zones: evidence from whole-rock geochemistry and Sr–Nd–Mo isotopes of the Paleogene Linzizong volcanic succession in southern Tibet. *J. Geophys. Res. Solid Earth* **124**, 456–475 (2019).
70. Mo, X. X. et al. Contribution of syn-collisional felsic magmatism to continental crust growth: a case study of the Paleogene Linzizong volcanic succession in southern Tibet. *Chem. Geol.* **250**, 49–67 (2008).
71. Zhou, S. et al. ⁴⁰Ar–³⁹Ar geochronology of Cenozoic Linzizong volcanic rocks from Linzhou Basin, Tibet, China, and their geological implications. *Chin. Sci. Bull.* **49**, 1970–1979 (2004).
72. Dong, G. C. *Linzizong Volcanic Rocks and Implications for Probing India Eurasia Collision Process in Linzhou Volcanic Basin, Tibet*. PhD thesis, China Univ. Geosciences, Beijing (2002).
73. Workman, R. K. & Hart, S. R. Major and trace element composition of the depleted MORB mantle (DMM). *Earth Planet. Sci. Lett.* **231**, 53–72 (2005).
74. Richards, A. et al. Himalayan architecture constrained by isotopic tracers from clastic sediments. *Earth Planet. Sci. Lett.* **236**, 773–796 (2005).
75. Aizawa, Y., Tatsumi, Y. & Yamada, H. Element transport by dehydration of subducted sediments: implication for arc and ocean island magmatism. *Island Arc* **8**, 38–46 (1999).
76. Tatsumi, Y. & Hanyu, T. Geochemical modeling of dehydration and partial melting of subducting lithosphere: toward a comprehensive understanding of high-Mg andesite formation in the Setouchi volcanic belt, SW Japan. *Geochem. Geophys. Geosyst.* **4**, 1081 (2003).
77. Hermann, J. & Spandler, C. J. Sediment melts at sub-arc depths: an experimental study. *J. Petrology* **49**, 717–740 (2008).
78. Wilson, M. *Igneous Petrogenesis*. (Springer, 1989).
79. Faure, G. & Mensing, T. M. *Isotopes: Principles and Applications* (Wiley, 2005).
80. Cramer, F. et al. A comparison of numerical surface topography calculations in geodynamic modelling: an evaluation of the ‘sticky air’ method: modelling topography in geodynamics. *Geophys. J. Int.* **189**, 38–54 (2012).
81. Turcotte, D. L. & Schubert, G. *Geodynamics* (Cambridge Univ. Press, 2014).
82. Ranalli, G. *Rheology of the Earth* (Springer-Verlag, 2011).
83. Cai, F. L. et al. Late Triassic paleogeographic reconstruction along the Neo-Tethyan Ocean margins, southern Tibet. *Earth Planet. Sci. Lett.* **435**, 105–114 (2016).

84. Hennig, J., Hall, R. & Armstrong, R. A. U-Pb zircon geochronology of rocks from west Central Sulawesi, Indonesia: extension-related metamorphism and magmatism during the early stages of mountain building. *Gondwana Res.* **32**, 41–63 (2016).
85. Wang, J. G. et al. Upper Triassic turbidites of the northern Tethyan Himalaya (Langjixue Group): the terminal of a sediment-routing system sourced in the Gondwanide Orogen. *Gondwana Res.* **34**, 84–98 (2016).
86. Mitchell, N. C. Modeling Cenozoic sedimentation in the central equatorial Pacific and implications for true polar wander. *J. Geophys. Res. Solid Earth* **103**, 17749–17766 (1998).
87. Savoye, B., Babonneau, N., Dennielou, B. & Bez, M. Geological overview of the Angola-Congo margin, the Congo deep-sea fan and its submarine valleys. *Deep Sea Res. PT II* **56**, 2169–2182 (2009).
88. Clift, P. & Vannucchi, P. Controls on tectonic accretion versus erosion in subduction zones: implications for the origin and recycling of the continental crust. *Rev. Geophys.* **42**, 2003RG000127 (2004).
89. Hu, X. M., An, W., Garzanti, E. & Liu, Q. Recognition of trench basins in collisional orogens: insights from the Yarlung Zangbo suture zone in southern Tibet. *Sci. China Earth Sci.* **63**, 2017–2028 (2020).
90. Noda, A. Forearc basins: types, geometries, and relationships to subduction zone dynamics. *Geol. Soc. Am. Bull.* **128**, 879–895 (2016).
91. Straub, S. M., Gómez-Tuena, A. & Vannucchi, P. Subduction erosion and arc volcanism. *Nat. Rev. Earth Environ.* **1**, 574–589 (2020).
92. Zhou, H. et al. Data from: India-Eurasia convergence speed-up by passive-margin sediment subduction. Dryad <https://doi.org/10.5061/dryad.8kpr4xwr> (2024).
93. Irvine, T. N. & Baragar, W. R. A. A guide to the chemical classification of the common volcanic rocks. *Can. J. Earth Sci.* **8**, 523–548 (1971).
94. Peccerillo, A. & Taylor, S. R. Geochemistry of eocene calc-alkaline volcanic rocks from the Kastamonu area, Northern Turkey. *Contrib. Mineral. Petrol.* **58**, 63–81 (1976).
95. Hasterok, D. et al. New maps of global geological provinces and tectonic plates. *Earth Sci. Rev.* **231**, 104069 (2022).
96. Den Hartog, S. A. M., Niemeijer, A. R. & Spiers, C. J. New constraints on megathrust slip stability under subduction zone P–T conditions. *Earth Planet. Sci. Lett.* **353–354**, 240–252 (2012).
97. Di Toro, G. et al. Fault lubrication during earthquakes. *Nature* **471**, 494–498 (2011).
98. Tsutsumi, A. & Shimamoto, T. High-velocity frictional properties of gabbro. *Geophys. Res. Lett.* **24**, 699–702 (1997).
99. Chester, F. M. & Higgs, N. G. Multimechanism friction constitutive model for ultrafine quartz gouge at hypocentral conditions. *J. Geophys. Res. Solid Earth* **97**, 1859–1870 (1992).
100. Del Gaudio, P. et al. Frictional melting of peridotite and seismic slip. *J. Geophys. Res. Solid Earth* **114**, B06306 (2009).
101. Schultz, R. A. Limits on strength and deformation properties of jointed basaltic rock masses. *Rock Mech. Rock Eng.* **28**, 1–15 (1995).

Acknowledgements J.H. is supported by the National Natural Science Foundation of China (NSFC) through awards 92155307, 92355302 and 42174106, and by the National Key R&D Program of China through awards 2023YFF0806300 and 2023YFF0803200. L.D.Z. is supported by the European Research Council (ERC) Synergy Grant ‘Fault Activation and Earthquake Rupture’ (FEAR) (No 856559), the Earth Observatory of Singapore (EOS) and the Singapore Ministry of Education Tier 3b project ‘Investigating Volcano and Earthquake Science and Technology (InVEST)’ (Award No. MOE-MOET32021-0002). Computations were supported by the Center for Computational Science and Engineering of the Southern University of Science and Technology. This paper benefitted from the efficient editorial handling by J. VanDecar. We thank K.X. and F.G. for their assistance with geochemical modelling.

Author contributions J.H. conceived and oversaw the study. H.Z. performed the numerical experiments and the geochemical analysis. L.D.Z. and K.L. provided valuable support on numerical modelling. X.H. provided valuable advice on sedimentology. M.T. provided valuable advice on geochemical analysis. All the authors participated in manuscript preparation.

Competing interests The authors declare no competing interests.

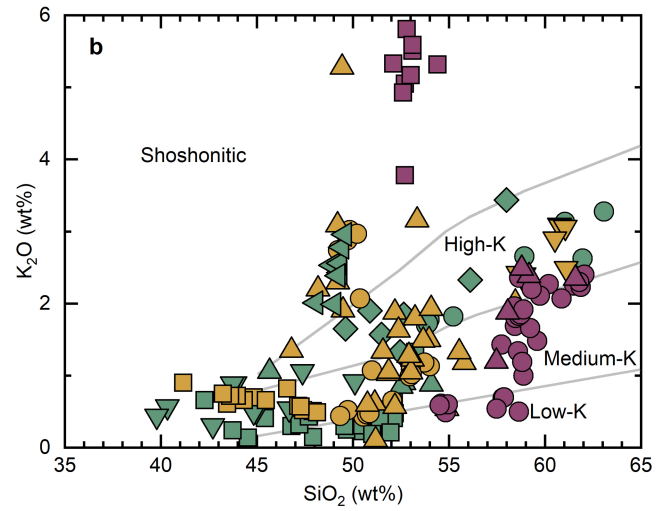
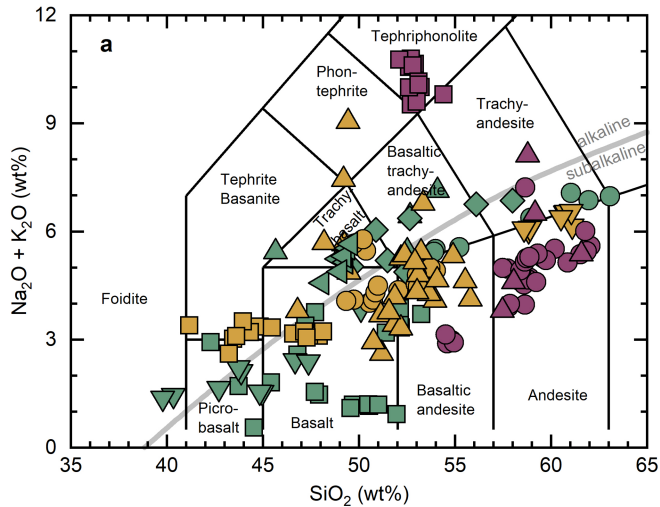
Additional information

Supplementary information The online version contains supplementary material available at <https://doi.org/10.1038/s41586-024-08069-6>.

Correspondence and requests for materials should be addressed to Jiashun Hu.

Peer review information *Nature* thanks Julie Prytulak and the other, anonymous, reviewer(s) for their contribution to the peer review of this work.

Reprints and permissions information is available at <http://www.nature.com/reprints>.



Group 1: samples >65 Ma

- *Ma et al., 2013a*
- *Meng et al., 2021*
- ▲ *Guan et al., 2011*
- ▼ *Ma et al., 2013b*
- ◆ *Tang et al., 2019*
- ◀ *Lei et al., 2021*

Group 2: samples 65-60 Ma

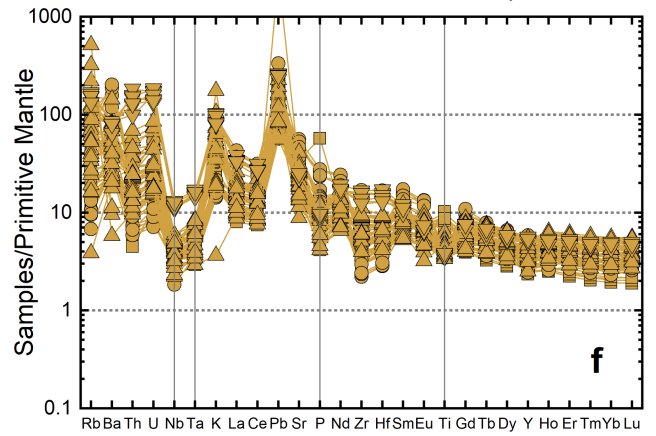
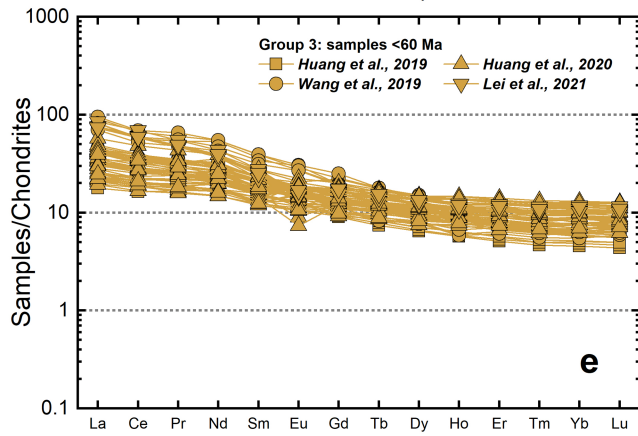
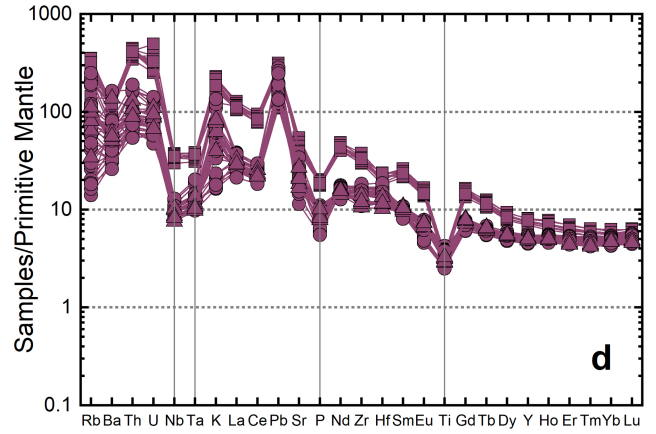
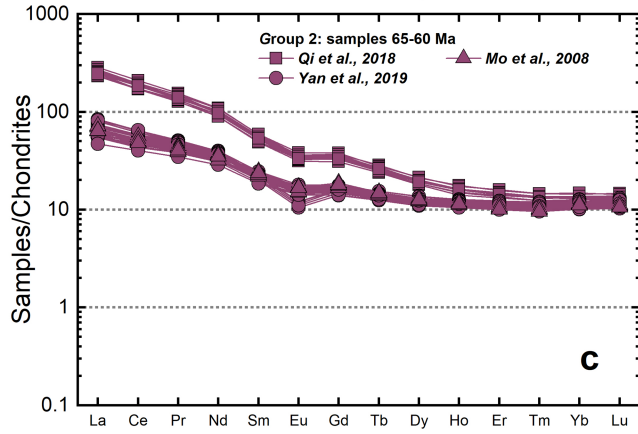
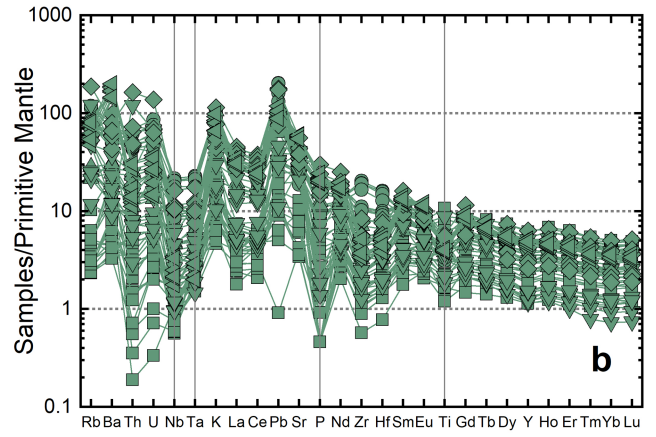
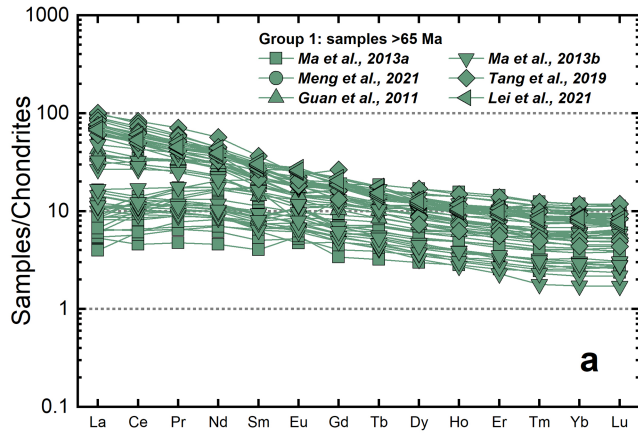
- *Qi et al., 2018*
- *Yan et al., 2019*
- ▲ *Mo et al., 2008*

Group 3: samples <60 Ma

- *Huang et al., 2019*
- *Wang et al., 2019*
- ▲ *Huang et al., 2020*
- ▼ *Lei et al., 2021*

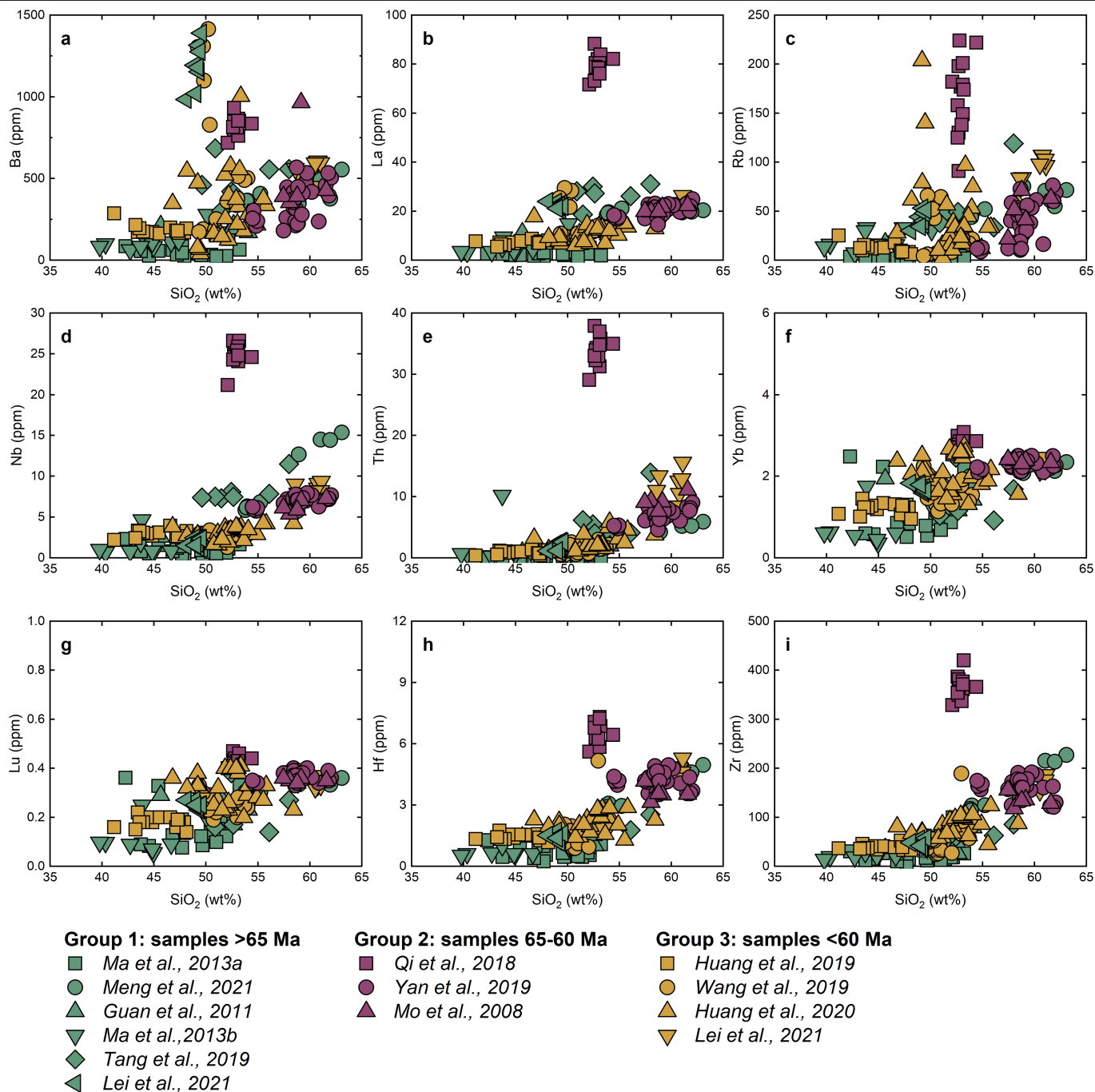
Extended Data Fig. 1 | Selected major element contents vs SiO_2 (wt%).
a, $\text{K}_2\text{O} + \text{Na}_2\text{O}$ (wt%) vs SiO_2 (wt%). Classification boundaries are from Irvine and Baragar (1971)⁹³. **b,** K_2O (wt%) vs SiO_2 (wt%). The dividing lines denote the

classification boundaries from Peccerillo and Taylor (1976)⁹⁴. Filled symbols represent, respectively, data from the published literature⁵⁹⁻⁷⁰.



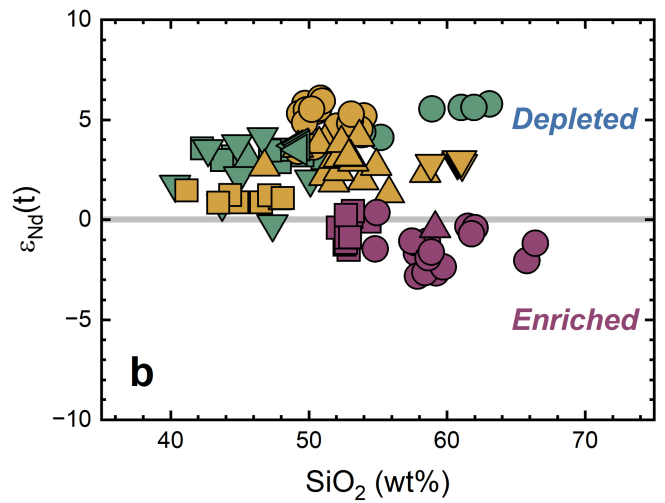
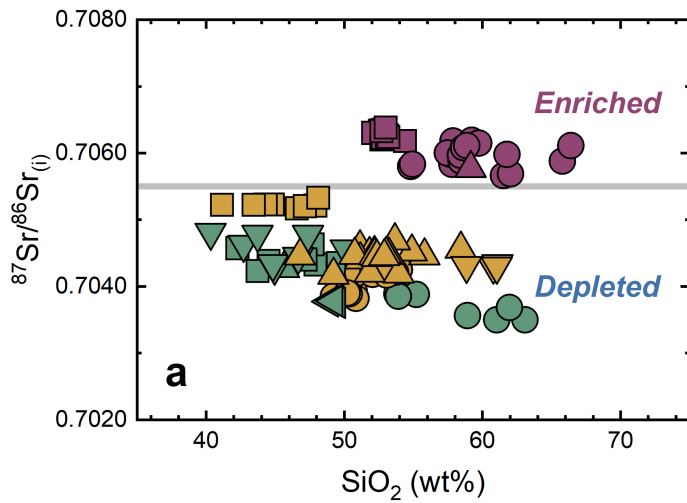
Extended Data Fig. 2 | Chondrite-normalized rare earth element patterns (left side) and primitive mantle normalized trace element diagrams (right side) for the Late Cretaceous–Early Cenozoic magmatic rocks of the

Gangdese arc. a–b, samples older than 65 Ma. c–d, samples between 65 and 60 Ma. e–f, samples younger than 60 Ma.



Extended Data Fig. 3 | Selected trace element contents versus SiO₂ values for Late Cretaceous-Early Cenozoic magmatic rocks from the Gangdese arc. Data sources are the same as those in Extended Data Fig. 1. The rock SiO₂ values for the Gangdese arc show vertical or lateral covariation patterns with

trace element concentrations within individual locations. This strongly indicates that such variations do not result from fractional crystallization (AFC) of a homogeneous primitive arc melt but reflect the compositional heterogeneity of primitive arc melts.



Group 1: samples >65 Ma

- *Ma et al., 2013a*
- *Meng et al., 2021*
- ▲ *Guan et al., 2011*
- ▼ *Ma et al., 2013b*
- ◆ *Tang et al., 2019*
- ◀ *Lei et al., 2021*

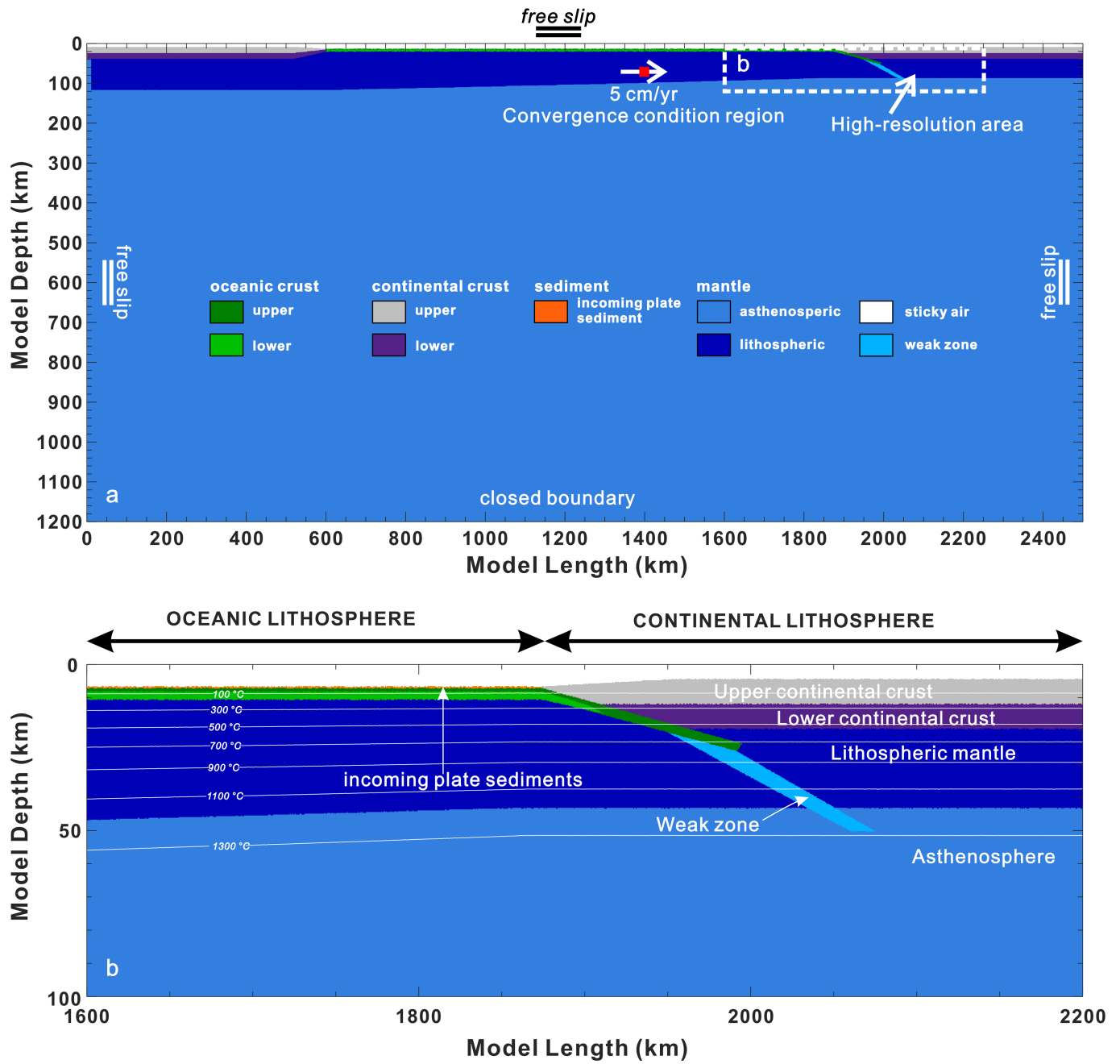
Group 2: samples 65-60 Ma

- *Qi et al., 2018*
- *Yan et al., 2019*
- ▲ *Mo et al., 2008*

Group 3: samples <60 Ma

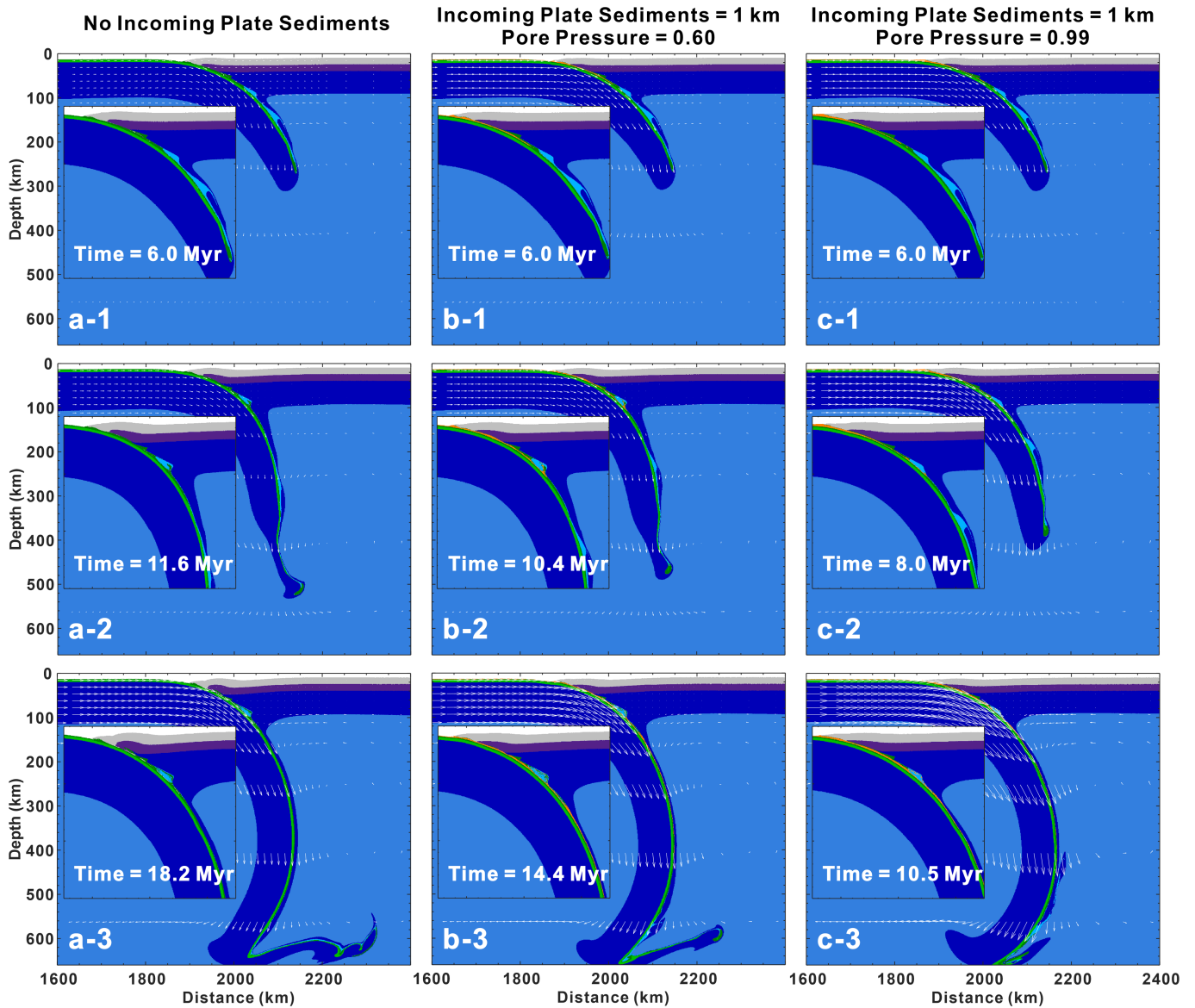
- *Huang et al., 2019*
- *Wang et al., 2019*
- ▲ *Huang et al., 2020*
- ▼ *Lei et al., 2021*

Extended Data Fig. 4 | Diagrams of whole-rock $^{87}\text{Sr}/^{86}\text{Sr}(t)$ and $\epsilon_{\text{Nd}}(t)$ values versus SiO_2 contents for Late Cretaceous-Early Cenozoic magmatic rocks from the Gangdese arc. Samples from the literature do not exhibit negative or positive covariation patterns between whole rock $^{87}\text{Sr}/^{86}\text{Sr}(t)$, $\epsilon_{\text{Nd}}(t)$ values, and SiO_2 contents.



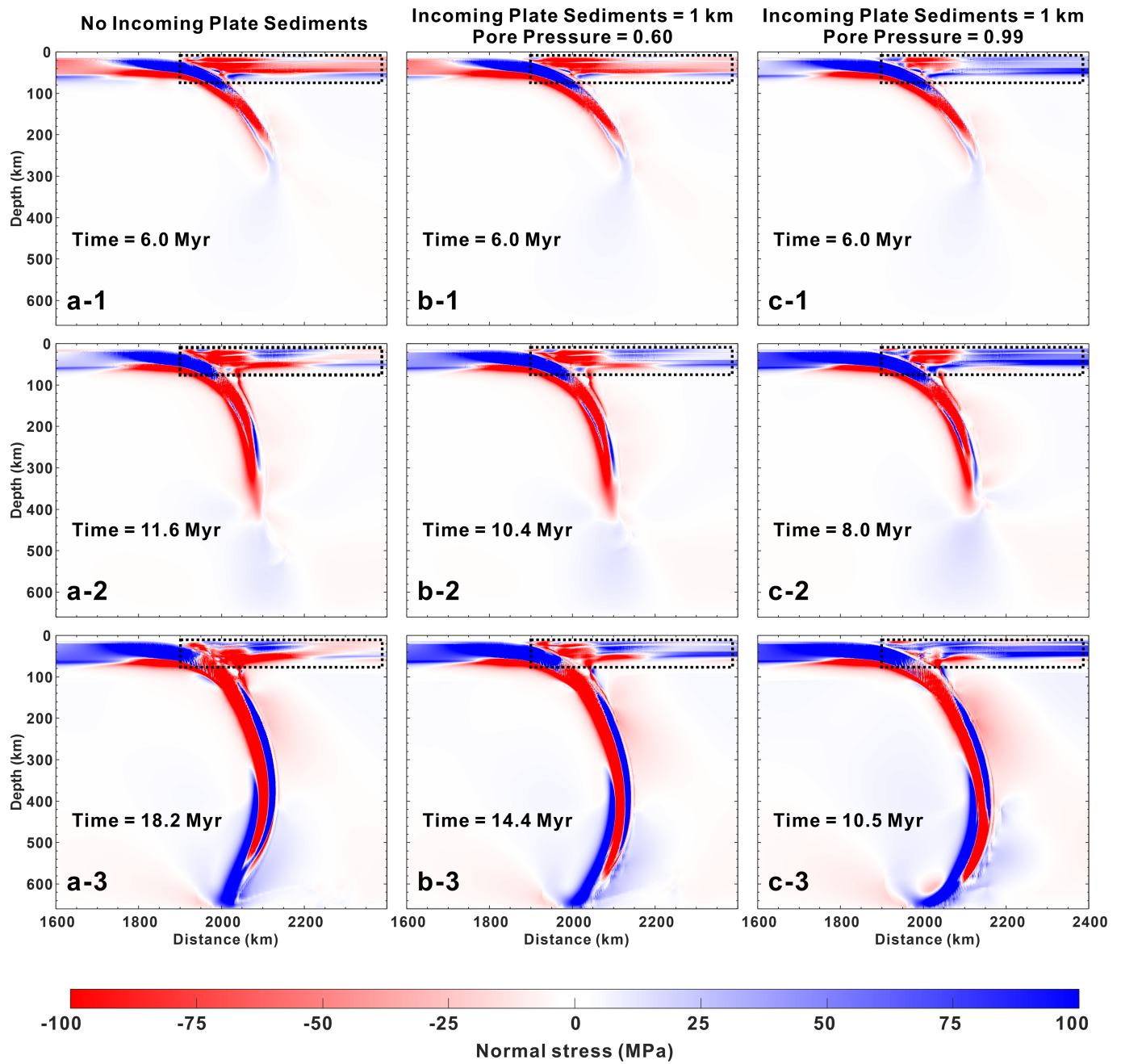
Extended Data Fig. 5 | Modeling setup of the two-dimensional numerical experiments. **a.** Compositional map of the whole computational domain (2500 × 1200 km). The initial slab is generated by imposing a fixed velocity

(white arrow) on a small region (red rectangle) of the subducting plate until 300 km of oceanic lithosphere has subducted. **b.** Zoomed-in version of the high-resolution area.



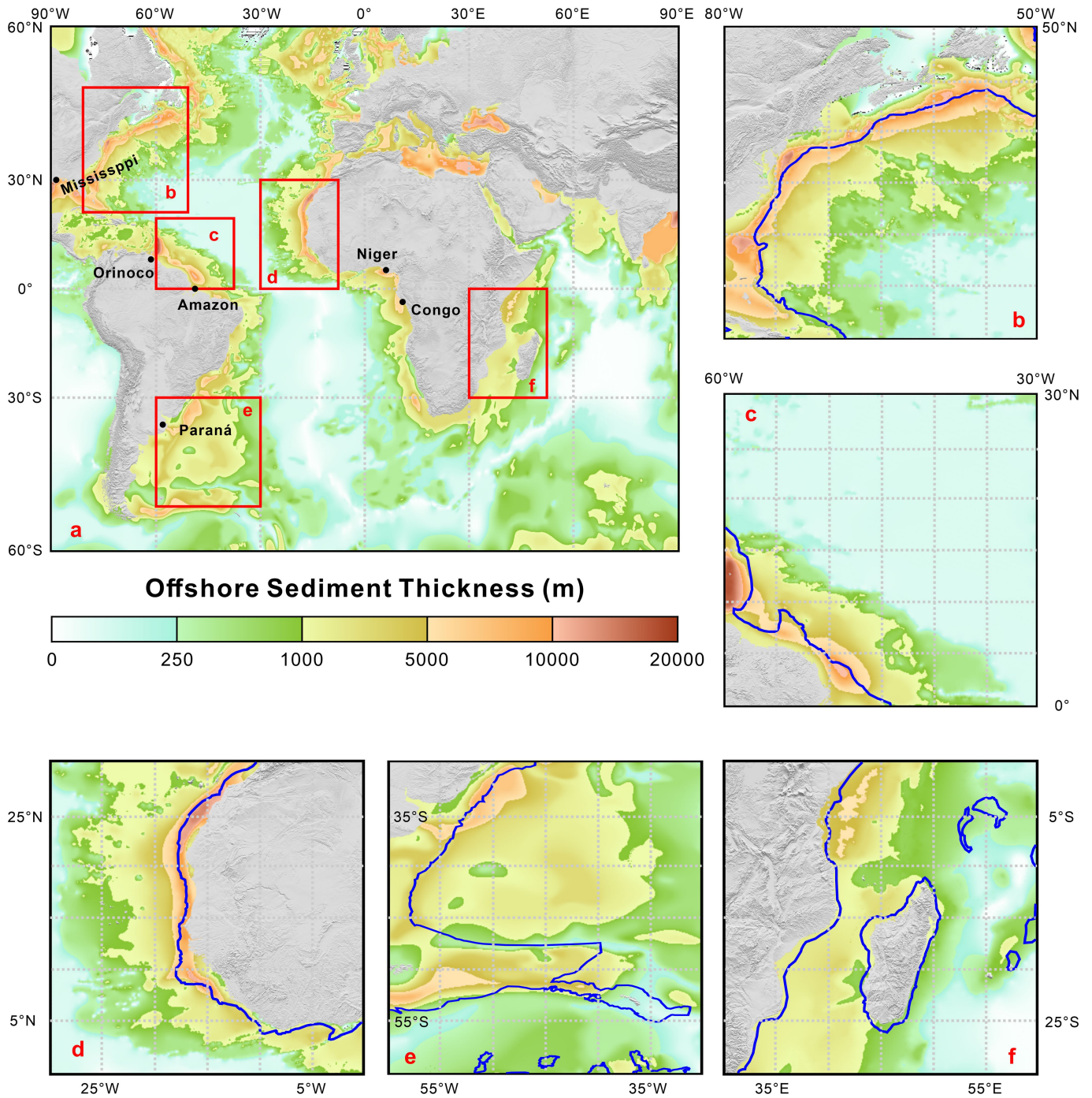
Extended Data Fig. 6 | Compositional fields of the models. **a**, no incoming plate sediments, **b**, 1 km-thick incoming plate sediments with pore pressure 0.60, and **c**, 1 km-thick incoming plate sediments with pore pressure 0.99 roughly at the stages of the (1) kinematically constrained subduction, (2) free

slab sinking, and (3) interaction with the 660 km discontinuity. The slab lengths corresponding to the three stages are 300 km, 400 km and 800 km respectively. The white arrows represent the direction and magnitude of the velocity.



Extended Data Fig. 7 | Horizontal stress map of the models. **a**, no incoming plate sediments, **b**, 1 km-thick incoming plate sediments with pore pressure of 0.60, and **c**, 1 km-thick incoming plate sediments with pore pressure of 0.90 roughly at the stages of the (1) kinematically constrained subduction, (2) free

slab sinking, and (3) interaction with the 660 km discontinuity. The slab lengths corresponding to the three stages are 300 km, 400 km and 800 km respectively. In this figure, a positive stress indicates an extensional tectonic setting, and a negative stress indicates a compressional tectonic setting.



Extended Data Fig. 8 | Global total sediment thickness. a, deep sedimentary basins straddle the rifted continental margins, especially at high-discharge river mouths (shown in black). Sediment thickness depicts data from

Straume et al.⁴⁴. b-f, sediment thickness map for different areas in Extended Data Fig. 8a, the solid blue line represents the ocean-continent boundary⁹⁵.

Article

Extended Data Table 1 | The elemental and isotopic compositions of the end-members for Sr-Nd isotope binary mixing simulation

End- members	Elements (ppm)		Isotopes	
	Sr	Nd	$^{87}\text{Sr}/^{86}\text{Sr}_{(i)}$	$\epsilon_{\text{Nd}}(t)$
Subducted sediments (Tethys-Himalaya)				
	46.4	32.7	0.753141	-18.09
	297	25.7	0.733451	-16.27
	99.7	34	0.761221	-13.32
	229	13	0.735692	-7.42
	93	33.7	0.758542	-13.67
	38	43.6	0.775981	-16.08
	61	25.7	0.773708	-15.73
	87	33.3	0.752422	-11.29
	67	25	0.774694	-12.94
	53	25.7	0.774423	-14.88
	63	32.3	0.765592	-12.90
	85	46.8	0.754544	-13.31
Subducted sediments (High-Himalaya)				
	135	29.9	0.740053	-16.88
	76.3	47.6	0.768227	-7.43
	120	31.2	0.747841	-15.10
	86	32.4	0.738382	-12.49
	122	29.7	0.740685	-12.22
	51.3	40.5	0.760685	-15.78
	121	23.3	0.747635	-15.04
	72.7	22.2	0.729667	-15.54
Depleted Mantle (DM)				
	7.664	0.581	0.702630	9.60

The trace element and radiogenic isotope compositions of DM are after Workman and Hart (2005)⁷³. The trace element and radiogenic isotope compositions for the subducted sediments (Tethys-Himalaya and High-Himalaya) are reported by Richards et al.⁷⁴, and the radiogenic isotope compositions data are both age-corrected to 70 Ma.

Extended Data Table 2 | Physical properties of rocks used in numerical experiments^{81,82,96-101}

Material	ρ_0 (kg/m³)	Thermal conductivity (W/m/K at T_k, P_{MPa})	Flow law
Incoming plate sediment	2800	$1.18+474/(T+77) \times \exp(0.00004P)$	Wet quartzite, $A=1.97 \times 10^{17}$ Pa s, $n=2.3$, $E=154000$ J/mol, $V=8$ J/mol/MPa, $C=1$ MPa, $u_s=0.35$, pore pressure=0.60-0.99
Upper oceanic crust (basalt)	3000	$1.18+474/(T+77) \times \exp(0.00004P)$	Wet quartzite, $A=1.97 \times 10^{17}$ Pa s, $n=2.3$, $E=154000$ J/mol, $V=8$ J/mol/MPa, $C=1$ MPa, $u_s=0.60$, pore pressure=0.60
Lower oceanic crust (gabbro)	3000	$1.18+474/(T+77) \times \exp(0.00004P)$	Plagioclase, $A=4.80 \times 10^{22}$ Pa s, $n=3.2$, $E=238000$ J/mol, $V=8$ J/mol/MPa, $C=1$ MPa, $u_s=0.85$, pore pressure=0.40
Upper continental crust	2700	$1.18+474/(T+77) \times \exp(0.00004P)$	Wet quartzite, $A=1.97 \times 10^{17}$ Pa s, $n=2.3$, $E=154000$ J/mol, $V=12$ J/mol/MPa, $C=1$ MPa, $u_s=0.72$, pore pressure=0.40
Lower continental crust	3000	$1.18+474/(T+77) \times \exp(0.00004P)$	Granulite, $A=1.25 \times 10^{21}$ Pa s, $n=4.2$, $E=445000$ J/mol, $V=8$ J/mol/MPa, $C=1$ MPa, $u_s=0.25$, pore pressure=0.00
Lithospheric mantle	3300	$0.73+1293/(T+77) \times \exp(0.00004P)$	Dry olivine, $A=3.98 \times 10^{16}$ Pa s, $n=3.5$, $E=532000$ J/mol, $V=8$ J/mol/MPa, $C=1$ MPa, $u_s=0.60$, pore pressure=0.00
Asthenospheric mantle	3300	$0.73+1293/(T+77) \times \exp(0.00004P)$	Dry olivine, $A=3.98 \times 10^{16}$ Pa s, $n=3.5$, $E=532000$ J/mol, $V=8$ J/mol/MPa, $C=1$ MPa, $u_s=0.60$, pore pressure=0.00
Weak zone mantle	3200	$0.73+1293/(T+77) \times \exp(0.00004P)$	Wet olivine, $A=5.01 \times 10^{20}$ Pa s, $n=4.0$, $E=470000$ J/mol, $V=8$ J/mol/MPa, $C=1$ MPa, $u_s=0.00$, pore pressure=0.40

η_0 is the reference viscosity; n is the stress exponent; E_a is the activation energy; V_a is the activation volume; ρ_0 is the reference density; G is the shear modulus; μ_s is the static friction coefficient, and C is cohesion.